Geoscience Frontiers 17 (2026) 102283

Contents lists available at ScienceDirect

Geoscience Frontiers

journal homepage: www.elsevier.com/locate/gsf

Research Paper

Timescales and magma dynamics of the plumbing system feeding a Plinian eruption: the 79 CE eruption of Somma-Vesuvius, Italy

Pierangelo Romano [a], Carlo Pelullo [b,*], Sumit Chakraborty [c], Andrea Luca Rizzo [d,e], Hélène Balcone-Boissard [f], Domenico Sparice [b], Domenico Maria Doronzo [b], Mauro Antonio Di Vito [b], Ilenia Arienzo [b]

[a] Istituto Nazionale di Geofisica e Vulcanologia, Sezione di Palermo, Via Ugo la Malfa, 153, Palermo 90146, Italy
[b] Istituto Nazionale di Geofisica e Vulcanologia, Osservatorio Vesuviano, Via Diocleziano, 328, Napoli 80125, Italy
[c] Institut für Geologie, Mineralogie und Geophysik, Ruhr Universität Bochum, Universitätsstraße 150, Bochum 44801, Germany
[d] Dipartimento di Scienze dell'Ambiente e della Terra, Università degli Studi di Milano-Bicocca, Piazza della Scienza, 4, Milano 20126, Italy
[e] Istituto Nazionale di Geofisica e Vulcanologia, Sezione di Milano, Via Alfonso Corti, 12, Milano 20133, Italy
[f] Sorbonne Université, Institut des Sciences de la Terre de Paris, CY – université, CNRS, 4 place Jussieu, Paris 75005, France

ARTICLE INFO

Article history:
Received 9 October 2025
Revised 27 December 2025
Accepted 7 February 2026
Available online 12 February 2026

Keywords:
Plinian eruption
Clinopyroxene zoning
Diffusion chronometry
Thermodynamic modelling
Isotope geochemistry
Plumbing system
Eruptive precursors

ABSTRACT

Plinian eruptions are the most common high impact explosive events, causing severe local impacts and influencing human settlement or migration and global climate. Understanding their pre-eruptive processes and timescales is crucial for forecasting eruptions and mitigating hazards. The iconic 79 CE Somma-Vesuvius eruption (Italy) is considered the archetype of Plinian eruptions. However, knowledge of its plumbing system architecture and pre-eruptive magmatic processes remains incomplete. Chemical and isotopic data, clinopyroxene zoning analysis, and numerical modelling reveal a vertically extended plumbing system with deep mafic magma batches refilling a tephri-phonolitic reservoir multiple times before the eruption. Diffusion modelling constrains recharge events in timescales from decades to less than a year, which align with historically well-documented seismicity ("*non desiit enim assidue tremere Campania*", Seneca; "*Praecesserat per multos dies tremor terrae*", Pliny the Younger) preceding the eruption. These findings enhance our understanding of volcanic behaviour, aiding in hazard assessment and risk mitigation for future similar eruptions.

1. Introduction

Plinian-type eruptions encompass a wide energetic interval in the spectrum of explosive activity, from micro-Plinian to ultra-Plinian eruptions (e.g. Giordano et al., 2024), and can have devastating local and global consequences. Historically, such eruptions have led to mass evacuations, economic loss, and in some cases, to destruction of entire cities, health issues and loss of life (Self, 2006; Baxter et al., 2015; Jay, 2024).

In this paper, we focus on the 79 CE Somma-Vesuvius eruption, also known as Pompeii eruption, which is well-known for being the archetype of Plinian eruption due to the thorough description provided by Pliny the Younger (*Epistulae* VI.16–20), after whom this type of large explosive activity was named. Somma-Vesuvius'activity has threatened communities that have been living around the volcano for millennia (e.g., Di Vito et al., 2019, 2023; Sparice et al., 2025). Nowadays ~700,000 people are living in the *peri*-volcanic area (https://www.protezionecivile.gov.it/it/approfondimento/aggiornamento-del-piano-nazionale-di-protezione-civile-il-vesuvio/#, n.d.) and are exposed to a significant volcanic risk.

In recent decades, knowledge of Somma-Vesuvius eruptive history and its eruption impacts has advanced significantly (e.g., Sbrana et al., 2020). Substantial progresses have been made in understanding magma evolution through open-system processes, the role of clinopyroxenes in differentiation, volatile contents and magma storage conditions, carbonate assimilation, and magma residence times (Civetta et al., 1991; Santacroce et al., 1993; Cioni et al., 1995, 1998; Marianelli et al., 1995; Black et al., 1998; Landi et al., 1999; Cioni, 2000; Morgan et al., 2006; Fulignati and Marianelli, 2007; Iacono-Marziano et al., 2007, 2009; Scaillet et al., 2008; Scheibner et al., 2008; Dallai et al., 2011; Balcone-Boissard et al., 2012, 2016; Pichavant et al., 2014; Buono et al., 2020; Wotzlaw et al., 2022; Esposito et al., 2023).

* Corresponding author.
E-mail address: carlo.pelullo@ingv.it (C. Pelullo).

https://doi.org/10.1016/j.gsf.2026.102283

Previous studies on the 79 CE eruption (Barberi et al., 1981; Sigurdsson et al., 1985, 1990; Joron et al., 1987; Civetta et al., 1991; Cioni et al., 1992, 1995; Marianelli et al., 1995; Cioni, 2000; Morgan et al., 2006; Piochi et al., 2006; Balcone-Boissard et al., 2008; Santacroce et al., 2008; Scaillet et al., 2008; Dallai et al., 2011; Melluso et al., 2022; Doronzo et al., 2023; Esposito et al., 2023; Fedele et al., 2025) detailed the geochemical and petrographic variations within the pyroclastic sequence and investigated the magmatic processes preceding the eruption. Despite all previous investigations, a detailed picture of what was happening beneath Somma-Vesuvius in the period leading up to the 79 CE eruption is missing. A deeper knowledge of the mechanisms governing the evolution of the plumbing system prior to the possible escalation toward an eruption is crucial to improve volcanic hazard assessment and enhance risk mitigation.

It is now known that magmatic processes occurring in transcrustal magmatic systems may trigger volcanic eruptions and affect their style (Blundy and Cashman, 2008; Petrone et al., 2016; Sparks and Cashman, 2017; Cooper, 2019). Several studies that investigated pre-eruptive processes were able to determine both the conditions and durations of pre-eruptive storage of magmas and the timescales of processes (i.e. magma differentiation, recharge and mixing processes) leading to magma assembly or mush disruption and then to the eruption (Heumann et al., 2002; Vazquez and Reid, 2004; Humphreys et al., 2006; Ginibre et al., 2007; Turner and Costa, 2007; Streck, 2008; Claiborne et al., 2010; Petrone et al., 2016, 2018, 2022; Ubide et al., 2019; Solaro et al., 2020; Ostorero et al., 2022).

The dynamics — and the relative evolution — of magma within the crust can be investigated utilizing approaches that allow the temporal changes in crystallisation conditions to be modeled. It is possible to reconstruct the crystallisation history of zoned crystals using the concept of magmatic environments (ME) that was introduced by Kahl et al. (2011, 2015) and has been widely used since then (e.g., Solaro et al., 2020; Ostorero et al., 2022; Pelullo et al., 2022, 2024). In a nutshell, the concept considers a specific composition of a given mineral to form as a consequence of one particular set of imposed relevant thermodynamic intensive variables (e.g. P, T, fO_2, fH_2O). This set of values define the magmatic environment (ME). This is an abstract quantity, unrelated to the physical nature of the magma reservoir (e.g., within the same physical reservoir there may be different magmatic environments, as in the case of a zoned magma chamber; or different physical reservoirs that are connected in a plumbing system may be different magmatic environments). The strength of the approach comes from the abstract general nature of the quantity because inferences about conditions and the timescales over which these changes are independent of assumptions about the physical nature of magma storage. Thus, a plateau (area characterized by a specific brightness in a BSE image and by a homogeneous composition, or by a very weak variation typically 15–20 μm long) in a compositional profile across a crystal indicates growth of that particular part of the crystal at a constant set of conditions, in one ME; jumps in concentrations represent sudden (with respect to rate of crystal growth) changes in one or more of the intensive variables that define a ME. The sequence of MEs recorded in a crystal zoning pattern tracks the passage of that crystal through different environments within a plumbing system; a statistical compilation of several crystals allows the pre-eruptive magma dynamics within the plumbing system to be deciphered. During the residence of a crystal in different MEs and its passage between them at high temperatures diffusion occurs to smooth the compositional gradients. Diffusion models provide constraints on the timescales of residence in different MEs, and/or transitions between them. More details are available in Costa et al. (2008) and Kahl et al. (2015). Subsequently, these may be related to physical processes such as mafic recharge, magma ascent, and movement at different depths that are essential parameters for the understanding of eruption behavior and hazard evaluation (Morgan et al., 2004; Costa et al., 2013; Kilgour et al., 2014; Dohmen et al., 2017; Flaherty et al., 2018; Petrone et al., 2018, 2022; Di Stefano et al., 2020; Mangler et al., 2020; Palummo et al., 2021; Pelullo et al., 2022, 2024; Nardini et al., 2024). The knowledge gained from such investigation aids in reconstructing future scenarios for volcanic eruptions and therefore in developing strategies for hazard assessment and risk mitigation (Kahl et al., 2015; Ostorero et al., 2022; Elms et al., 2023; Polo-Sánchez et al., 2023).

In this work, chemical and isotopic data, high-spatial resolution analyses of zoned clinopyroxene from selected 79 CE eruptive units, numerical modelling of magma evolution (Rhyolite- MELTS code) and Fe-Mg diffusion modelling applied to crystal zoning were used for reconstructing the evolution of magmas that fed the eruption. This approach allowed us to gather information on (i) the magmatic feeding system architecture and on (ii) the types and timescales of magmatic processes leading to this Plinian event. We provide a multifaceted comprehensive view of the magmatic system linking the long-lasting evolution of the magmas feeding the 79 CE to the last episodes of reservoir growth preceding the eruption, and we propose a correlation with seismic crises that occurred in the years before 79 CE. The knowledge of the behaviour of the volcano prior to large eruptions can contribute to the hazard assessment in such a densely populated area.

2. The 79 CE eruption: sampling and analytical rationale

The 79 CE eruption unfolded through three main phases: it started with an initial phreatomagmatic explosion, climaxed in the formation of an oscillating to collapsing eruption column (Plinian phase) and then ended with a caldera-forming to final phreatomagmatic phase. These dynamics resulted in a complex stratigraphy consisting of fall and pyroclastic current deposits (e.g. Sigurdsson et al., 1985; Cioni et al., 1990, 1992, 1999; Doronzo et al., 2022; Scarpati et al., 2024). In this paper, we rely on the stratigraphic framework of Cioni et al. (1990, 1992) who arranged the composite 79 CE succession in eight Eruption Units (EUs). A basal thin phreatomagmatic ash layer (EU1) is overlaid by a Plinian fall deposit characterized by an upward colour variation from white phonolitic (EU2f) to grey tephri-phonolitic (EU3f) pumice. The fall deposit is interspersed with pyroclastic current ash deposits (EU3pf sub-units) associated with several partial collapses of the Plinian column, and covered by a complex succession of pyroclastic current deposits interstratified with thin lithic-rich fall layers (EU3pftot to EU8). These deposits are associated with pyroclastic fountaining following the ultimate collapse of the eruption column (EU3pftot), beginning and climax of caldera collapse (EU4 to EU6) and final phreato-magmatic phase (EU7 and EU8) punctuated by brief resumptions of a post-Plinian eruption column (Scarpati et al., 2024). Due to the extremely sectoral and narrow dispersal of some units (e.g., Gurioli et al., 1999; Doronzo et al., 2022; Scarpati et al., 2024), a complete type section of the 79 CE deposits is not available. Based on literature data, Pozzelle quarry (40.796935°N, 14.467026°E), in the municipality of Terzigno, 4.5 km south-east of the current Vesuvius crater, has been selected for sampling. The selected site is representative of most of the 79 CE pyroclastic sequence, as it is located well inside the dispersal area of the Plinian fall deposit as well as in the area inundated by part of the intra-Plinian and all post-Plinian pyroclastic currents (Scarpati et al., 2024). The sampled stratigraphic sequence at Pozzelle quarry (Fig. 1) is composed of 7 out of 8 EUs (EU5 is the less dispersed unit), resting on brown paleosols, and attaining a total thickness between 10 and more than 20 m

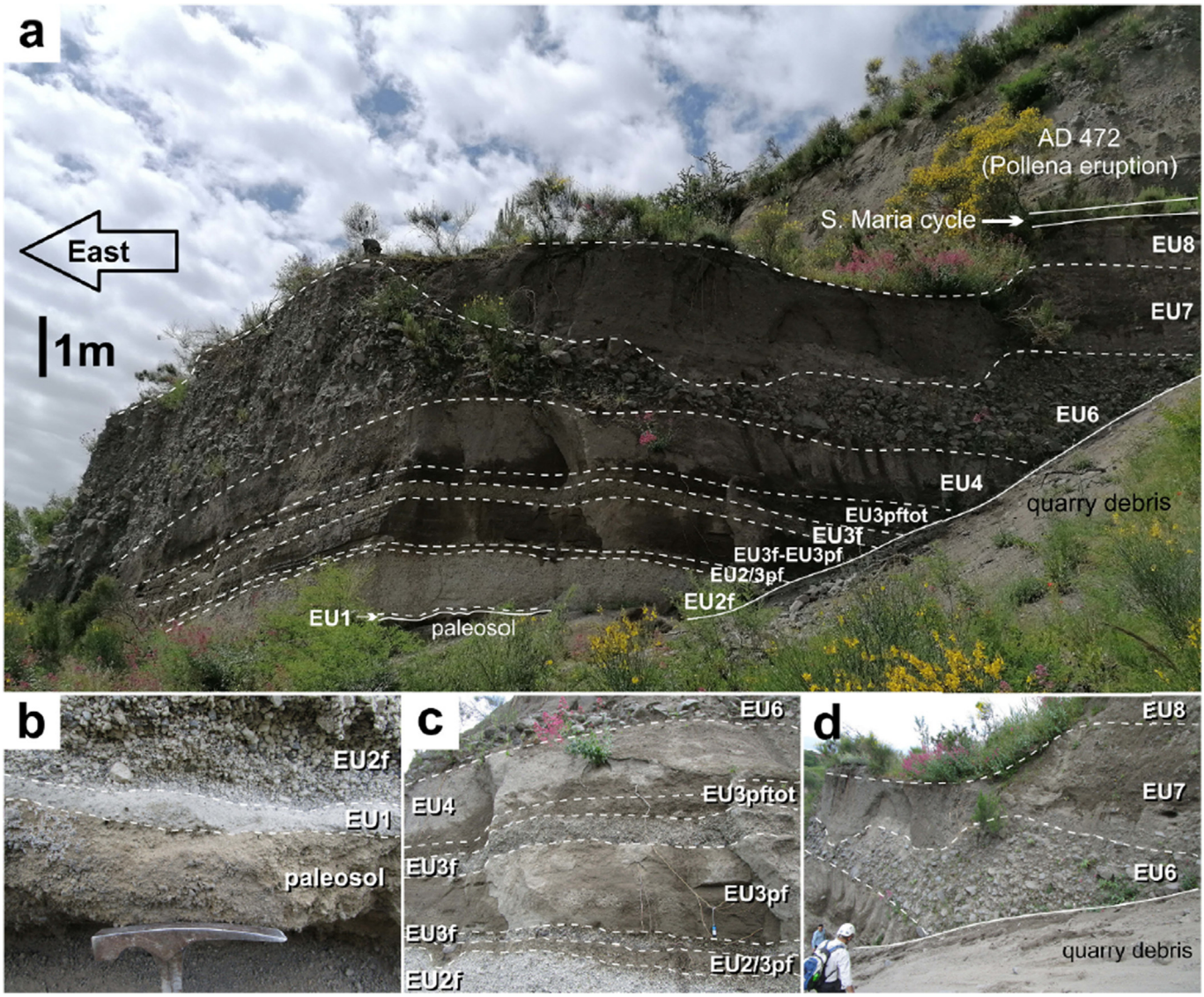

Fig. 1. Photos of the stratigraphic sequence of the 79 CE eruption at Pozzelle quarry (Terzigno) modified from Doronzo et al. (2022) and Scarpati et al. (2024). (a) Panoramic view of the stratigraphic sequence (EU1 to EU8). (b) Detail of the basal part of the sequence (EU1 to EU2f); (c) detail of the middle part of the sequence (EU2f to EU6; EU5 is lacking in this exposure being the less dispersed unit); (d) detail of the upper part of the sequence (EU6 to EU8).

(Doronzo et al., 2022; Scarpati et al., 2024). Samples representative of the componentry (juvenile) of each unit were collected throughout the sequence.

3. Material and methods

Density measurements, bulk major and trace elements, isotopic (Sr and Nd) and mineral chemistry analyses were carried out on pumice samples (samples labelled "VT-79" followed by the corresponding unit) and two mafic cumulates (samples VT-C1 and VT-C2 sampled in EU3fC base unit) vertically from the whole stratigraphic sequence (Table 1; Supplementary Data Tables S1–S3).

Moreover, $^{3}He/^{4}He$ and $\delta^{13}C$ isotopic analyses were performed on fluid inclusions in minerals from mafic cumulate fragments and from the grey pumices.

The whole dataset provides a comprehensive record of the physical and compositional variability between grey and white pumices. Details on sample preparation, density measurements, chemical and isotopic analyses are given below and in Supplementary Material (Samples and Methods).

Pumice samples belonging to the EU2f and EU3f (VT-79 EU2f top and VT-79 EU3fB) eruptive units show the widest variability in terms of density, chemical and isotopic composition, and thus have been selected for the zoning pattern characterization and diffusion modelling. The two selected samples consist of weakly porphyritic pumice fragments. Sample VT-79 EU2f top (white pumices) is vesicular and characterized by a few small phenocrysts — mainly sanidine with minor green clinopyroxene, garnet, leucite, phlogopite, amphibole, plagioclase and opaque minerals — and displays a glassy groundmass. Sample VT-79 EU3fB is less vesicular and contains more abundant phenocrysts of sanidine and clinopyroxene along with phlogopite, amphibole, and rare olivine, and shows microlitic textures in the groundmass.

Pumices were washed in distilled water, and then dried at 110 °C. Later, these were gently crushed through a jaw crusher and sieved. Grain size fractions between 0.025 mm and 1 mm were inspected under a stereo microscope for picking up clinopyroxene crystals. Selected crystals within the 0.5–1 mm range were embedded in epoxy resin and polished for scanning electron microscope (SEM) inspection and electron microprobe analyses (EMPA). About

Table 1
List of the 79 CE Eruptive Units (EU) and related samples. The analyses performed on each sample are shown.

Pumice colour	Eruptive unit	Sample	Whole rock analyses	Sr-Nd isotopic ratios	Mineral chemistry	Compositional profiles in Cpx	Density measurements	Noble gases and CO_2
	EU8	VT-79 EU8	x					
	EU7	VT 79 EU7 base	x	x				
	EU6	VT-79 EU6	x					
	EU4	VT-79 EU4pf						
	EU3pftot	VT-79 EU3pftot base	x					
	EU3f	VT-79 EU3fC top	x	x	x			x
	EU3f	VT-79 EU3fC base	x				x	
	EU3pf	VT-79 EU3pf top	x					
	EU3pf	VT-79 EU3pf base	x					
Grey p.	EU3f	VT-79 EU3fB	x	x	x	x	x	
Grey p.	EU3f	VT-79 EU3fAtop					x	
Grey p.	EU3f	VT-79 EU3fAbase	x				x	
.	EU2/3pf	VT-79 EU2/3pf						
White p.	EU2f	VT-79 EU2f top	x	x	x	x	x	
White p.	EU2f	VT-79 EU2f mid	x					
White p.	EU2f	VT-79 EU2f base	x	x	x		x	
White p.	EU1	VT-79 EU1						
M.cum	EU3f	VT-C1		x	x			x
M.cum	EU3f	VT-C2			x			x

Note: Grey p. = grey pumices; White p. = white pumices; M.cum = mafic cumulate.

220 clinopyroxenes were separated from pumice samples and about 50 from cumulate samples. Compositional core-to-rim traverses were acquired on clinopyroxenes belonging to the EU2f and EU3f eruptive units. The quantitative compositional profiles were measured on 35 crystals showing optical evidence of compositional zoning (Supplementary Data Table S4). Among the 35 analysed clinopyroxenes, 13 crystals belong to sample VT-79 EU2f top and 22 crystals belong to sample VT-79 EU3fB.

3.1. EMP analyses

Mineral compositions were obtained at the HP-HT Laboratory of Experimental Volcanology and Geophysics of the Istituto Nazionale di Geofisica e Vulcanologia in Rome (Italy), using a Jeol-JXA8200 electron microprobe equipped with five wavelength dispersive spectrometers and performing single spot analyses on both unzoned and zoned crystals and core-to-rim transects on zoned clinopyroxene crystals. Crystals were analysed under high vacuum conditions, using an accelerating voltage of 15 kV and a beam current of 7.5 nA. Spot dimension varies between 2 and 3 μm in diameter. The compositional transects in zoned clinopyroxenes were realized with 3 to 6 μm spots separation and length of transects varies between 18 and 300 μm depending on the zoning pattern. Elemental counting times were 10 s on the peak and 5 s on each of two background positions. Corrections for inter-elemental effects were made using a ZAF (Z: atomic number; A: absorption; F: fluorescence) routine. The range of standards for calibration was taken from Micro-Analysis Consultants (https://www.mac-standards.co.uk, n.d.) (MAC) and variable diffraction devices: albite (Si-PET, Al-TAP, Na-TAP), forsterite (Mg-TAP), augite (Fe-LIF), apatite (Ca-PET), orthoclase (K-PET), rutile (Ti-PET) and rhodonite (Mn-LIF). Accuracy was better than 1%–5% except for elements with abundances below 1 wt.%, for which it was better than 5%–10%. Precision was typically better than 1%–5% for all analysed elements.

3.2. Diffusion modelling

Diffusion modelling was performed only on crystals showing suitable conditions, i.e. not on crystals showing intricate textures (patchy zoning) and complex Al vs Mg# relations. The diffusion equation

$$\frac{dC}{dt} = \frac{d}{dx}\left(D(t)\frac{dC}{dx}\right) \quad (1)$$

describes how concentration gradients (i.e., concentration profiles: dC/dx) evolve as a function of time (t) and was solved with the Finite difference method to determine the time (t). The diffusion coefficient, based on Fe-Mg interdiffusion rates in clinopyroxene obtained by Müller et al. (2013), was calculated using the expression:

$$D^{Fe-Mg} = 2.77 \pm 4.27 \times 10^{-7} exp\left(\frac{-320.7 \pm 16\ \mathrm{kJ/mol}}{RT}\right) \mathrm{m^2/s} \quad (2)$$

where R is the gas constant and T is the temperature in Kelvin.

The compositional (Mg#, Al_2O_3) plateaus found in the crystals were used to infer the initial profile shapes before the diffusive modification. Based on the different behaviours shown by the Mg# vs Al_2O_3 content in the core to rim profiles, two different methods were used for diffusion modelling. Overall, these parameters show a linear anti-correlation (e.g., Fig. 2) related to magma evolution (e.g., fractional crystallisation). A detailed analysis of the single profiles shows subtle differences (Fig. 2a and b).

Most crystals display a good correlation (Fig. 2c). This correlation can be used to infer the hypothetical initial Mg# profile that is plotted in Fig. 2e. The measured profile (black diamonds in Fig. 2e) and the theoretical profile (red diamonds in Fig. 2e) are almost identical within the data's accuracy. This suggests that the Mg# profile experienced minimal, if any, Fe-Mg interdiffusion. Most profiles have a good Mg# vs Al_2O_3 (wt.%) correlation and, hence, exhibit negligible signs of diffusive modifications of growth zoning. They were used for classifying compositional populations in the zoning pattern (section 4.2) and for estimating an upper limit for the residence timescale using Method I. This limit may correspond to the maximum duration that the crystals could have remained in a magmatic environment at a given temperature, without detectable diffusive modification of the profiles (within the analytical resolution of this study; Chakraborty et al., 1991; Trepmann et al., 2004; Pelullo et al., 2022, 2024).

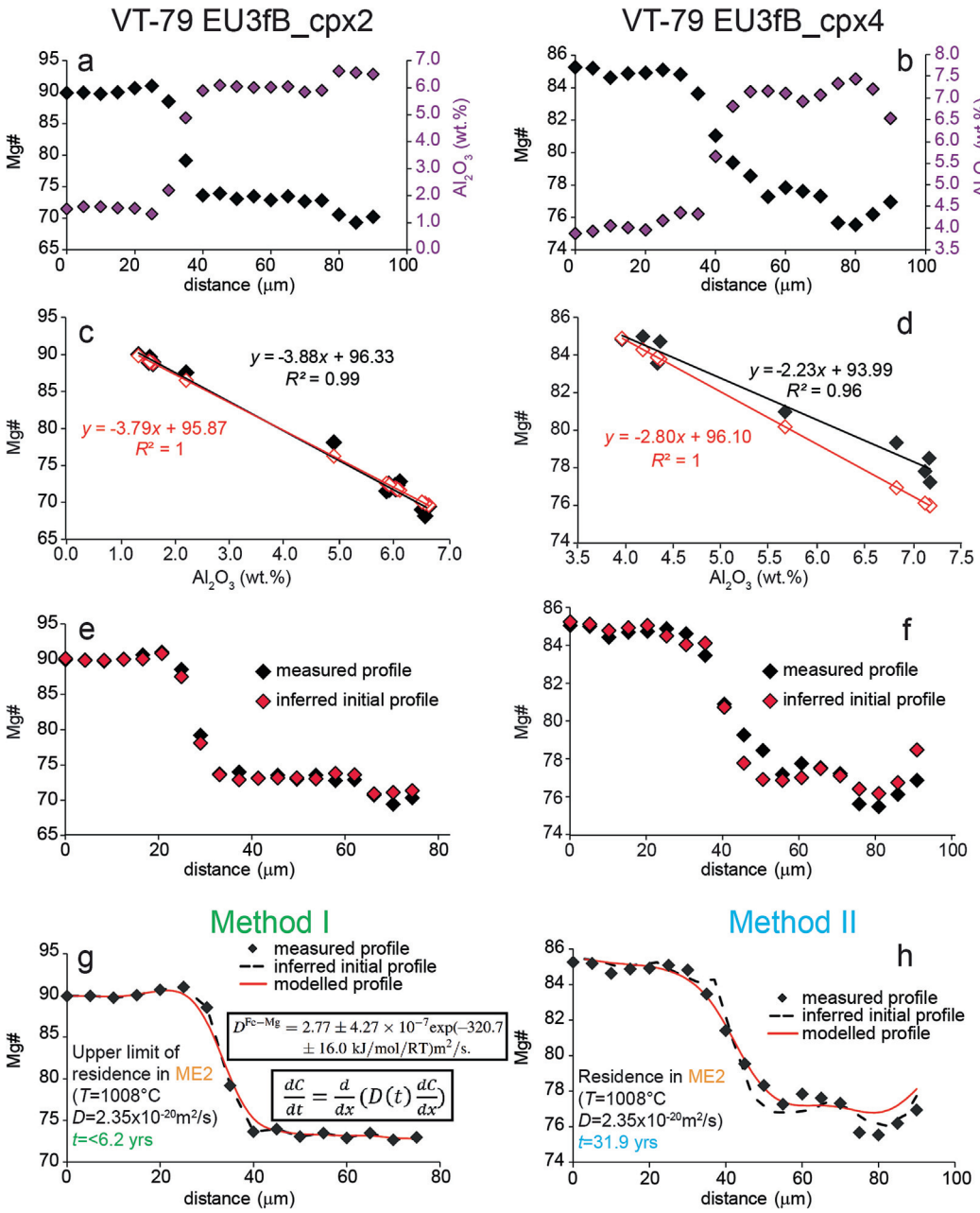

Fig. 2. Examples of the different behaviours of the Mg# vs Al_2O_3 content in the crystal profiles and associated diffusion modelling; (a, b) examples of Mg# and Al_2O_3 (wt.%) profiles of two selected crystals; the distance increases from core to rim; (c, d) Mg# vs Al_2O_3 (wt.%) relations of the two selected crystal profiles; (e, f) measured (black diamonds) and inferred (red diamonds) initial Mg# profiles calculated based on the relations assessed by best fit of the linear trendlines shown in panels (e and f); (g, h) examples of diffusion modelling applied to the selected crystals showing different relations between Mg# and Al_2O_3 (wt.%); black diamonds indicate the measured profiles; black dashed lines indicate the initial profile shapes: these are different depending on the relationships between Al_2O_3 (wt.%) and Mg# in the profiles; red lines indicate the modelled profiles.

In a few crystals, Al_2O_3 content and Mg# do not show a very good linear correlation (in Fig. 2d, the slope of the observed -black- and inferred -red- linear trendlines is different). In this case, the Al_2O_3 profile preserves a sharper gradient while the Mg# shows more smoothed concentration patterns (e.g., Fig. 2b). This indicates that the original concentration was affected by Fe-Mg interdiffusion. The crystals in which deviations in the correlation between Mg# and Al_2O_3 content are observed were modelled using Method II, yielding more reliable temporal constraints on the durations of residence of the crystals in a magmatic environment. The trendline of Fig. 2d is used to infer original initial Mg# profile that is shown in Fig. 2f. Such a theoretical initial Mg# profile (red diamonds in Fig. 2f) deviates from the measured profile (black diamonds in Fig. 2f), and the difference is more perceptible in the region of the compositional gradient. In agreement with the known different diffusion behaviour of Fe-Mg and Al in clinopyroxenes (Sautter et al., 1988; Müller et al., 2013), this points to the fact that the Mg# profiles have been affected by diffusion whereas Al was less affected (or not at all).

In Method I, the measured profiles are taken as the initial profiles, and Eqs. (1) and (2) are used to simulate the temporal evolution of the profile shapes. The timescales at which the calculated

profiles significantly differ from the initial profiles (Fig. 2g) are considered upper limits of the crystals' residence times in a specific magmatic environment.

In Method II, the Mg# profiles inferred on the Al_2O_3 contents (e.g., Fig. 2f) are taken as the initial profile shapes for Mg# and, through Eqs. (1) and (2), the timescales at which the calculated profiles fit the measured Mg# profiles (Fig. 2h) represent residence times in a specific magmatic environment. In both methods, solutions to the diffusion equation for suitable initial and boundary conditions are used. The boundary conditions may either be constant composition or no flux at the ends of the diffusion zones, with minimal impact on the results because the system behaves as an infinite diffusion couple.

4. Results

4.1. Chemical and Sr-Nd isotopic composition

The 79 CE whole rocks composition shows a clear variation in major and trace elements from the white phonolitic- to the grey tephri-phonolitic- pumices, as well as in density (Supplementary Material; Supplementary Data Table S1).

Results of the isotopic analyses show a variation from the first erupted white phonolitic pumices, featured by relatively high $^{87}Sr/^{86}Sr$ ratios, to the grey ones, relatively less enriched in radiogenic Sr. Crystals have variable Sr isotopic ratios. Among them, feldspars are more enriched in radiogenic Sr and are similar to the white pumices. Nd isotopes are similar, within the analytical error, from the base upward (Supplementary Material).

4.2. Clinopyroxene compositional populations and zoning patterns

Clinopyroxenes from the 79 CE eruption are diopsidic to Fe-salitic in composition ($Wo_{45-52}En_{16-49}Fs_{6-32}$) with small differences between those from the white and grey pumices (except for one crystal from the white pumices showing more Fe-rich composition; Supplementary Material; Supplementary Data Table S2).

Most (65%) of the 79 CE clinopyroxenes from pumice samples show optical evidence of zoning (Table 2).

In this study, for the zoned crystals, we use the term "mantle" to refer to the distinguishable plateaus between their core and rim (Fig. 3a). The zoned crystals typically (36%) present patchy zoned cores and, in minor part (29%), homogenous cores with mantles and rims typically forming concentric growth zones (Supplementary Data Fig. S5).

Moreover, the variation in the chemical composition along core-to-rim traverses highlights several zoning patterns (Fig. 3a and b) of clinopyroxene that are described below and in Supplementary Material (Section 2.5).

The unzoned crystals from pumice samples have Mg# in the range 76–92 and Al_2O_3 in the range of 1.3–5.8 wt.% (Fig. 3c).

Clinopyroxene crystals of mafic cumulates are all unzoned (Table 2), they mostly have very high Mg# (88–92) and low Al_2O_3 (1.4–2.5 wt.%) (Fig. 3c; Supplementary Data Fig. S4b–d).

Zoned clinopyroxene crystals, on which core-to-rim microanalyses were acquired, were selected from pumice samples representative of the white and grey pumices, which exhibit the most variable texture and chemical and isotopic compositions (Supplementary Material; Supplementary Data Figs. S1 and S2). In the samples VT-79 EU3fB (grey pumices) and VT-79 EU2f top (white pumices), 65% and 74% of the clinopyroxene crystals are zoned, respectively (Table 2).

The Mg# and Al_2O_3 content of the zoned crystals span wider compositional ranges (40–92 wt.% and 0.9–11.3 wt.%, respectively; Fig. 3c) with respect to those of the unzoned crystals.

The chemical composition of the zoned 79 CE clinopyroxene is made up of five compositional populations (MEs), clearly distinguishable based on the Mg# and the Al_2O_3 content and their occurrence in the different zones (core, mantle and rim) of the crystals (Fig. 3c):

- ME0 (Mg# = 87–92, Al_2O_3 = 1.0–2.2 wt.%) represents 36.5% of the analysed zoned crystals.
- ME1 (Mg# = 82–86, Al_2O_3 = 2.3–4.2 wt.%) accounts for 9.5%.
- ME2 (Mg# = 63–81, Al_2O_3 = 4.4–8.4 wt.%) is the most common, comprising 38.6%.
- ME3 and ME4 (Mg# = 50–62 and 39–46, both with Al_2O_3 = 8.6–11.2 wt.%) are less frequent, occurring in 13.6% and 2.2% of crystals, respectively.

Core compositions are dominated by ME0 (63%), followed by ME1 (17%), ME2 (9%) and ME3 (11%); no cores corresponding to ME4 were found.

Mantles, observed in 10 out of 35 analysed zoned crystals, display the following distribution: ME0 (22%), ME1 (12%), ME2 (44%), ME3 (16%), and ME4 (6%).

Rims are predominantly ME2 (71%), with minor contributions from ME3 (17%), and ME0/ME1 (6% each).

Together with Mg# and Al_2O_3 content, the classification into the above mentioned five MEs is largely corroborated by SiO_2, and Na_2O contents (Fig. 3d).

It is worth noting that ME0 and ME2 are the two most abundant compositions, representing about 75% of the compositions. ME0 is also the most frequent composition of the unzoned crystals from both pumices and cumulates (Fig. 2c). Notably, most cores (63%) of the zoned crystals have the ME0 composition, whereas ME2 is the most frequent composition in the rims (71%).

A schematic and comprehensive view of the 79 CE clinopyroxene zoning patterns is given by the system connectivity diagram (Fig. 4). In such statistical approach, MEs can be visualized as components of a petrological box model, where each box represents a distinct ME and each arrow (connecting two or more boxes) indicates the composition of a crystal from core to rim (Kahl et al., 2011, 2013, 2015; Solaro et al., 2020; Ostorero et al., 2022; Pelullo et al., 2022, 2024). The arrows in Fig. 4 show the chemical variation, in terms of MEs, from core (to mantle, if any) to crystal rim. It allows tracking the sequential growth of MEs in each crystal. As a result, it is possible to quantify the connections among various

Table 2
Number of observed crystals and percentages of zoned and unzoned clinopyroxenes for each pumice and mafic cumulate sample. The number of analysed profile for clinopyroxene crystals from the pumice samples is also reported.

Sample	Observed crystals	Unzoned	Zoned	Analysed crystals (along profiles)
EU3fB	206	73 (35%)	133 (65%)	22
EU2fA top	19	5 (26%)	14 (74%)	13
tot	225	78 (35%)	147 (65%)	35
VT-C1	33	33		
VT-C2	14	14		
tot	47	47 (100%)		

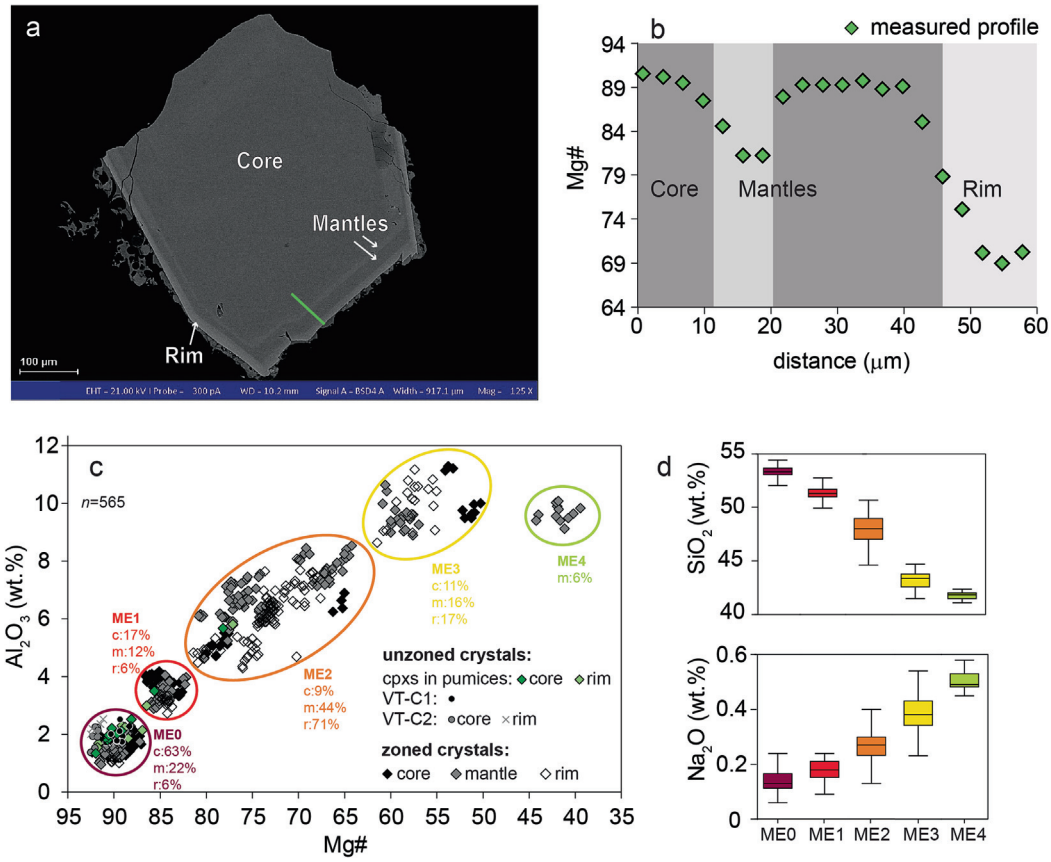

Fig. 3. (a) BSE image of a zoned clinopyroxene crystals from the 79 CE eruption showing several mantles between core and rim; (b) core-to-rim Mg# profile from the crystal in panel (a); green diamonds are points measured along the core-to-rim profile (indicated by a green line in the BSE images); (c) Mg# vs Al_2O_3 (wt.%) variation diagrams for core, mantle and rim of zoned clinopyroxene crystals. This allows different compositional populations (MEs) to be identified. The frequency of occurrence of each ME in the zones (c: core, m: mantle, r: rim) of the analysed clinopyroxenes is reported; it is based on the total number of zones of the 35 analysed crystals. The composition of the unzoned crystals is also plotted. (d) SiO_2, and Na_2O box plot diagrams showing the distinct clinopyroxene compositional populations; the upper and lower lines indicate the maximum and minimum values, respectively; the box encompasses the 95% of confidence intervals; the line within the box is the average of the values.

MEs through the entire set of zoning patterns, reconstructing the past history of conditions and processes.

Zoning patterns were distinguished in normal and reverse. Normal zoning is defined by the decrease of Mg# from core outwards (e.g., thick purple lines linking ME0 to ME2 in Fig. 4). Overall, 74% of the 35 analysed crystals show normally zoned cores. Reverse zoning, displayed by 26% of the analysed crystals, is characterized by Mg# increasing from core outwards (e.g., thick yellow lines from ME3 to ME2 in Fig. 3).

A great number of arrows among two or more MEs highlights common intracrystalline variations. Most of the connections are between ME0 and ME2 environments (thick purple lines). The connections, in some cases, are also from ME1 to ME0 to ME2. Some arrows connect ME3 (cores) and ME2 (rims) or ME0 and ME3, or ME1, ME2 and ME3 (in the form of normal and reverse-to-normal zoning). No ME other than ME3 is connected to ME4. A detailed description of the zoning in terms of MEs is in Supplementary Material (section 2.5).

4.3. Temperature conditions of clinopyroxene crystallisation

Crystallisation conditions of the 79 CE clinopyroxene were investigated using the thermometers of Masotta et al. (2013) and Bardeglinu et al. (2020). We considered the composition of MEs and, as regard the Masotta et al. (2013) geothermometer, both MEs and liquids in equilibrium with them (see Supplementary Material, section 2.6). We tested the equilibrium conditions for several clinopyroxene-melt couples belonging to the different MEs using the clinopyroxene-liquid equilibrium exchange coefficient obtained for Vesuvius magmas ($^{Fe-Mg}Kd_{Cpx\text{-}Liq}$ = 0.27 ± 0.06; Pichavant et al., 2014) and hypothetical melt compositions inferred from chemical analyses of whole rock, groundmass glass and melt inclusions taken from the literature (Cioni et al., 1995, 1998, 1999; Santacroce et al., 2008; Esposito et al., 2023) (Fig. 5; Supplementary Data Table S11). Both the white and grey pumices are weakly porphyritic to nearly aphyric (e.g., Fedele et al., 2025), hence the bulk chemical composition, due to not being significantly affected by the crystal content, is comparable to the groundmass glass composition. ME3 and ME4 compositional populations resulted in equilibrium with the phonolitic whole rocks and matrix glasses (Mg# = 17–32), ME2 and ME3 with the tephri-phonolitic whole rocks and melt inclusions with Mg# in the range 30–64, whereas ME1 and ME0 resulted in equilibrium only with melt inclusions with Mg# in the range 58–69 (Fig. 5a). Based on the clinopyroxene-melt equilibrium and clinopyroxene compositions, we calculated the crystallisation temperatures for each ME. The average temperatures (Fig. 5b; Supplementary Data Table S6) obtained with the Masotta et al. (2013) themometer for clinopyroxene of the compositional groups ME0 and ME1 are 1115 ± 6 °C and 1074 ± 7 °C, respectively. Almost identical values (1115 ± 6 °C for ME0 and 1086 ± 6 °C for ME1) were obtained following Bardeglinu et al. (2020). The ME2 clinopyroxenes (Mg# = 64–81) present average crystallisation temperatures of 1008 ± 31 °C (1026 ± 26 °C following Bardeglinu et al., 2020).

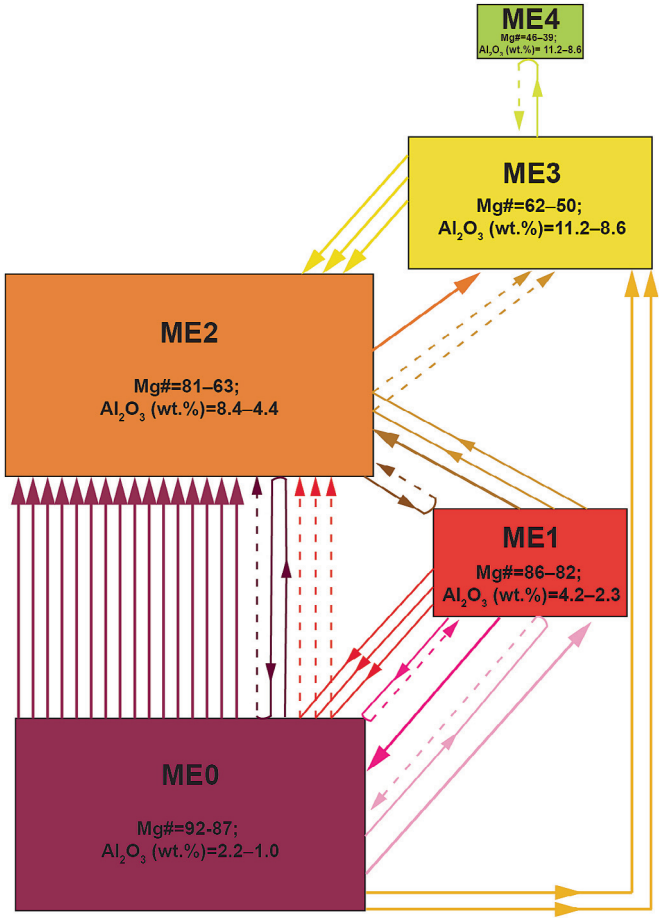

Fig. 4. System connectivity diagram of the 79 CE clinopyroxene zoning pattern. Each line indicates the core to rim composition along the analysed profiles; the size of the boxes is proportional to the frequency of occurrence of the MEs. Thick lines refer to core-rim transitions; thin lines refer to core-mantle transitions; thin dashed lines refer to mantle-rim transitions.

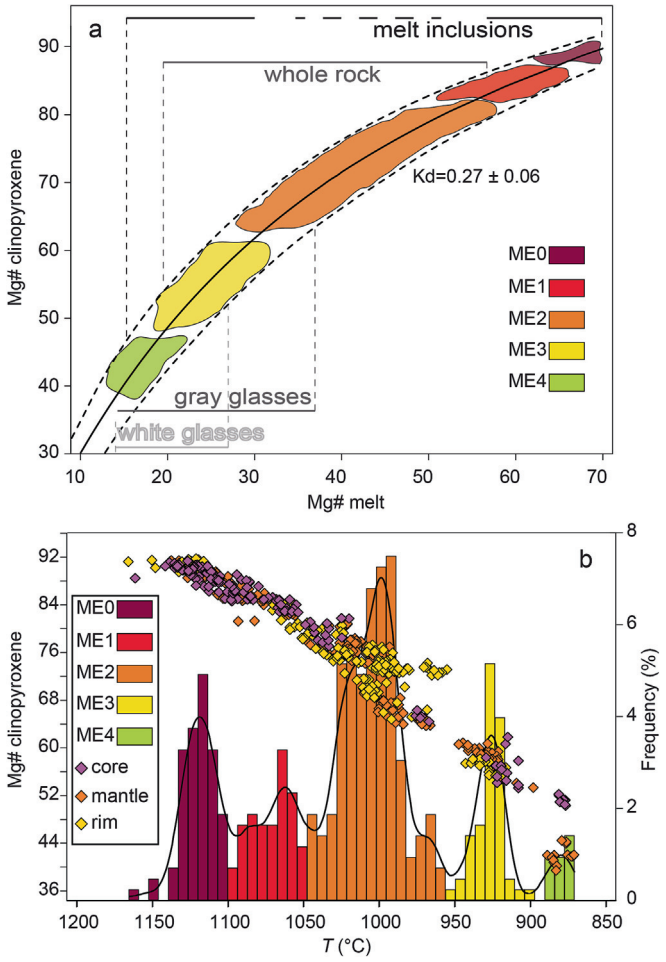

Fig. 5. Equilibrium test and temperature estimates for the 79 CE clinopyroxene-melt couples. (a) Test of equilibrium for the MEs of the 79 CE clinopyroxene based on the Fe–Mg partitioning ($^{Fe-Mg}Kd_{Cpx\text{-}Liq}$ = 0.27 ± 0.06; Pichavant et al., 2014) between clinopyroxene and host rock; continuous line is $^{Fe-Mg}Kd_{Cpx\text{-}liq}$ = 0.27; dotted lines = ± 0.06; (b) *T* (°C) vs clinopyroxene Mg# variation diagram and histogram of the calculated *T* values.

The ME3 (Mg# = 50–62) and ME4 (Mg# = 39–46) clinopyroxenes present average crystallization temperatures of 920 ± 21 °C and 882 ± 40 °C, respectively (933 ± 15 °C and 851 ± 10 °C, respectively, following Bardeglinu et al., 2020). The standard error of estimate (SEE) for the employed geothermometers are 18.2 (calibration SEE of Masotta et al., 2013) and 14.5 °C (Bardeglinu et al., 2020).

4.4. Noble gas and carbon isotopes in fluid inclusions in clinopyroxene

The results of elemental and isotopic analyses of helium ($^3He/^4He$ ratio), neon (^{20}Ne), argon ($^{40}Ar/^{36}Ar$), and CO_2 in fluid/melt inclusions hosted in olivine and clinopyroxene crystals from pumices and mafic cumulates are reported in Supplementary Data Table S5. Further information on noble gas concentrations are in Supplementary Material (section 2.4). The $^3He/^4He$ ratios corrected for the atmospheric contamination (expressed Rc/Ra) vary between 2.61 and 2.70 with a bias with the uncorrected $^3He/^4He$ ratios ≤ 0.1 Ra. The CO_2 concentrations in fluid inclusions hosted in olivine and clinopyroxene from pumices and mafic cumulates range from 2.1×10^{-10} to 4.3×10^{-8} mol g^{-1} (the highest values recorded by crystals in cumulates), with $CO_2/^3He$ ratios varying between 2.3×10^7 and 3.7×10^9. It is worth mentioning that in clinopyroxene from the cumulate sample VT-C1, the CO_2 concentration, quantified during crushing for noble gas analysis yielded values of 3.9×10^{-8}, comparable with those obtained during the crushing finalized to the carbon isotopic measurement (4.3×10^{-8} mol g^{-1}). The $\delta^{13}C$ value of the CO_2 in clinopyroxene from the cumulate is −3.8‰. No $\delta^{13}C$ values were determined on clinopyroxene from pumices due to the low CO_2 concentrations.

4.5. Modelling Vesuvius magma evolution

The rhyolite-MELTS code (v.1.2.0; Gualda et al., 2012; https://melts.ofm-research.org/) was employed to conduct thermodynamic simulations on the Vesuvius magmas. The MELTS thermodynamic approach has been successfully employed to estimate temperature, pressure and volatile content conditions during the crystallisation of mafic to silicic magmas of Campi Flegrei (Fowler et al., 2007; Pappalardo et al., 2008; Fowler and Spera, 2010; Cannatelli, 2012; Amstutz et al., 2025), Ischia (Brown et al., 2014) and Somma-Vesuvius (Pappalardo and Mastrolorenzo, 2010), among others. Approximately 100 fractional and equilibrium crystallisation models were run. The experimental glass 17–2 of Pichavant et al. (2014) was used to represent the initial mafic magma composition. This glass derives from a trachybasaltic glass equilibrated with olivine crystals (Fo_{90}) at 1200 °C, 2 kbar, redox conditions approximating QFM + 4, and containing 3 wt.% of H_2O and 1861 ppm of CO_2 dissolved in the melt. This composition is comparable to that of melt inclusions in Fo-rich olivine (Esposito et al., 2023), exhibiting a marginally higher MgO content. The best

fit with the 79 CE melt inclusions data taken from the literature (Fig. 6a and b) was achieved through the implementation of a multi-step equilibrium crystallisation model. This entailed the execution of equilibrium crystallisation at different *P*, *T*, and fO_2 conditions, aimed at reproducing the physico-chemical conditions of the recognized MEs, followed by the utilisation of the resulting liquid composition for the subsequent equilibration step. The equilibrium crystallisation steps were started at 1220 °C, 5 kbar and QFM + 2, and performed at progressively decreasing temperature (1220 to 840 °C), pressure (5 to 2.5 kbar) and redox conditions (QFM + 2 to QFM−1). Results of MELTS modelling are reported in Supplementary Data Tables S7–S10. We observed that a primitive (trachy-basaltic) liquid at 1220 °C and 5 kbar first crystallises olivine ($Fo_{89.3}$) followed by the cotectic crystallisation of clinopyroxene (with Mg# = 91.2) at 1200 °C (Fig. 6c). For temperature and pressure decreasing from 1220 to 1000 °C and from 5 to 2.5 kbar, respectively, melt evolution is driven by the crystallisation of olivine and clinopyroxene, whilst the melt composition attains Mg# in the range of 71.7–45.3 and a CaO/Al_2O_3 ratio within a 1.2–0.4 range. In this *T*-*P* range, the olivine composition exhibits a variation from $Fo_{89.3}$ to $Fo_{68.2}$, while the Mg# of clinopyroxene varies from 91.8 to 78 (Fig. 6d). At a pressure of 2.5 kbar and temperature below 1020 °C, biotite replaces olivine in the crystallisation sequence (Fig. 6c), while feldspar becomes stable at $T \leq 900$ °C. In the temperature range of 1000–840 °C, the composition of clinopyroxene evolves from Mg# = 78 to Mg# = 53 (Fig. 6d). It was not possible to perform MELTS simulations at temperatures below 840 °C and pressures of < 2.5 kbar.

4.6. Diffusion modelling

The kinetic modelling of the zoning patterns of the 79 CE clinopyroxene yields information on the crystals residence timescales in the different detected MEs. According to the equilibrium conditions and the results of thermometry (Fig. 5b), we used the average temperature representative of the ME occurring in the outer plateau of the modelled profile (i.e., 1008 °C for the ME2 rims in a core-rim or mantle-rim profile) in Eq. (2). It is worth noting that the two independent thermometric approaches and the MELTS simulations converge on comparable temperature estimates (Fig. 6d). Consequently, using temperatures derived from any of these models in the diffusion calculations would yield essentially similar timescale estimates. Eighteen out of 25 (Table 3) crystals were suitable to model the relaxation of growth zoning (Method I), while 7 crystals were suitable for modelling the residence times (Method II) (details in section 3.2).

The estimates obtained using Method I are less than 10 years, with 6 out of 18 crystals yielding durations of less than 2 years that

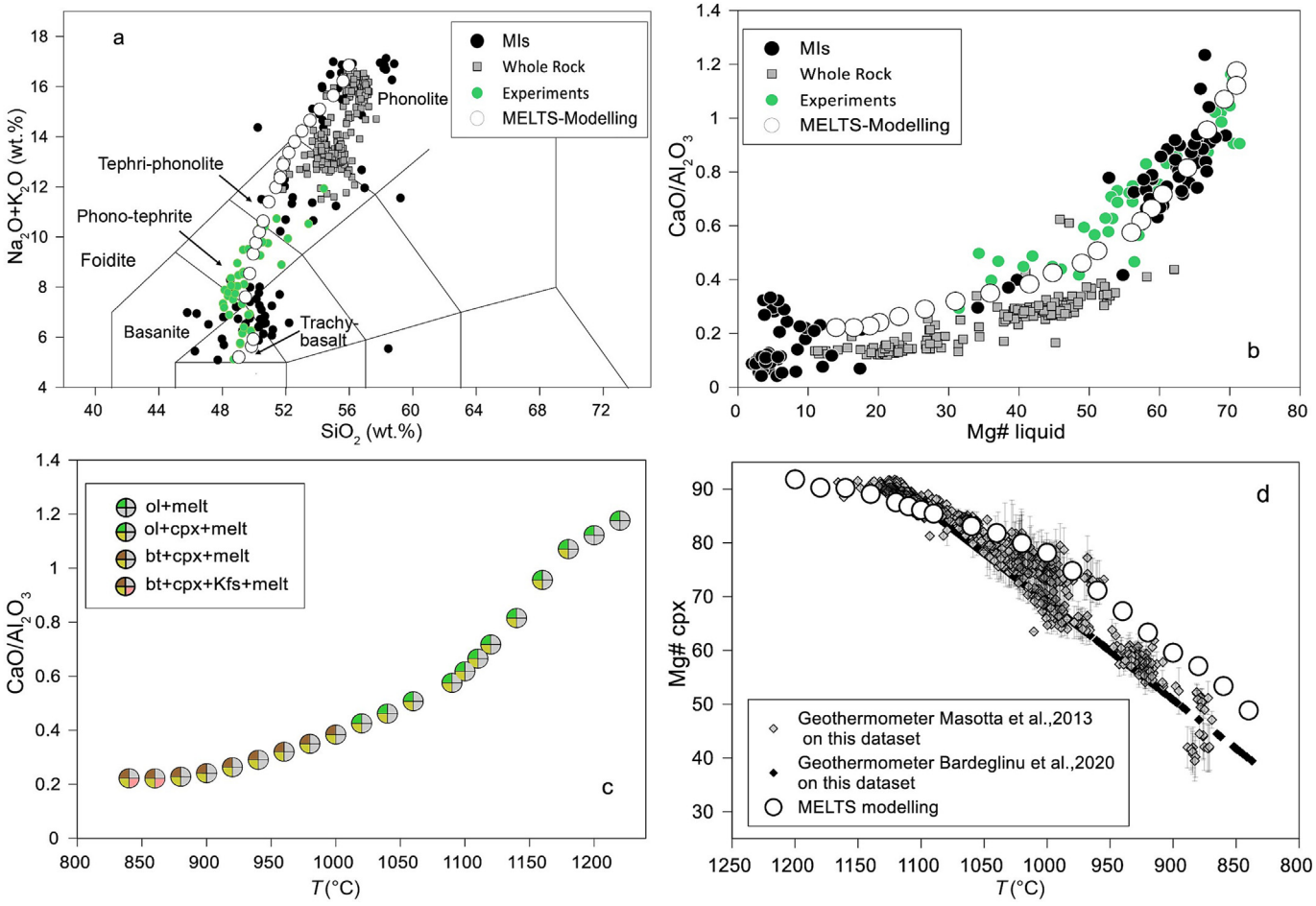

Fig. 6. Results of MELTS modelling compared with literature data and thermometric models. (a) Results of MELTS modelling plotted in the Total Alkali vs Silica diagram and compared with whole rocks (Santacroce et al., 2008), melt inclusions (Cioni et al., 1995, 1998; Marianelli et al., 1995; Cioni, 2000; Lima et al., 2007; Balcone-Boissard et al., 2008; Esposito et al., 2023) and experimental results (Pichavant et al., 2014); (b) Mg# vs CaO/Al_2O_3 of the 79 CE whole rocks, melt inclusions and experimental dataset compared with the liquid compositions calculated through MELTS software; (c) CaO/Al_2O_3 vs *T* (°C) of liquid compositions resulting from MELTS modelling, showing the mineral assemblages; ol: olivine, cpx: cplinopyroxene, bt: biotite, Kfs: alkali-feldspar; (d) Mg# of clinopyroxenes vs temperature calculated with both the geothermometers of Masotta et al. (2013) and Bardeglinu et al. (2020), compared with the result of MELTS calculations.

Table 3
Timescale (in years) estimates for the 79 CE clinopyroxene crystals derived from Fe-Mg diffusion modelling across selected transects. The timescales were calculated using the output temperatures obtained for the ME represented by the most external plateau of the crystals. In Method I, the measured profile is taken as the initial profile, whilst time in Eq. (1) (Section 3.2) is varied until the modelled profile diverges from the initial profile. This approach estimates the maximum extent of diffusive smoothing that a concentration (Mg#) profile has experienced, providing an upper limit to the residence times. In Method II, the shape of the initial profile is inferred based on the correlation between Al_2O_3 and Mg# (Fig. 2). Residence times are then determined by matching the modelled profile to the measured profile. In this case, error estimates (in brackets) were calculated based on the standard error of estimates of the thermometer (18.2 °C; Masotta et al., 2013); "stages" refer to crystals showing more than two growth zones/plateaus (e.g., core-mantle-rim) and on which sequential diffusion modelling was performed applying Method II; c = core, m = mantle, r = rim.

sample	cpx	step	Mg#	MEs step	zoning type	residence in	Method I	Method II	
								stages	total
VT-79 EU2f top	cpx2	c-r	55-75	ME3-ME2	reverse	ME2	**<1.5**		
	cpx3	c-m-r	83-90-73	ME1-ME0	reverse to normal	ME1	**<5.8**		
	cpx4	c-m	65-58	ME2-ME3	normal to normal	ME3		22.2	**27.7** (18.6-42.3)
		m-r	58-56	ME3-ME3		ME3		5.5	
	cpx5	c-m	82-77	ME1-ME2	normal	ME2	**<8.9**		
	cpx6	c-m	55-60	ME3-ME3	reverse to reverse	ME3		15.5	**25.6** (14.2-37.7)
		m-r	60-67	ME3-ME2		ME2		10.0	
	cpx8	c-r	90-73	ME0-ME2	normal	ME2	**<7.9**		
	cpx9	c-r	90-74	ME0-ME2	normal	ME2			**9.6** (6.3-14.1)
	cpx11	c-r	88-77	ME0-ME2	normal	ME2	**<2.5**		
VT-79 EU3B	cpx1	c-r	89-79	ME0-ME2	normal	ME2			**18.3** (10.9-25.0)
	cpx2	c-r	90-73	ME0-ME2	normal	ME2	**<6.2**		
	cpx3	c-m-r	90-85-91	ME0-ME1-ME0	normal to reverse	ME0	**<1.6**		
	cpx4	c-m	85-77	ME1-ME2	normal to normal	ME2		26.8	**31.9** (16.1-48.1)
		m-r	77-58	ME2-ME3		ME3		5.1	
	cpx6	c-r	60-76	ME3-ME2	reverse	ME2	**<4.9**		
	cpx8	c-r	90-73	ME0-ME2	normal	ME2	**<5.0**		
	cpx9	c-m-r	85-91-75	ME1-ME0-ME2	reverse to normal	ME2	**<5.8**		
	cpx10	c-r	90-72	ME0-ME2	normal	ME2			**23.7** (14.1-32.5)
	cpx12	c-r	89-74	ME0-ME2	normal	ME2			**8.9** (5.9-15.8)
	cpx13	c-r	90-75	ME0-ME2	normal	ME2	**<1.5**		
	cpx14	c-r	90-72	ME0-ME2	normal	ME2	**<7.7**		
	cpx15	c-r	90-72	ME0-ME2	normal	ME2	**<4.2**		
	cpx17	c-r	89-76	ME0-ME2	normal	ME2	**<2.5**		
	cpx18	c-r	86-73	ME1-ME2	normal	ME2	**<4.8**		
	cpx19	c-r	88-74	ME0-ME2	normal	ME2	**<1.9**		
	cpx20	c-m-r	83-89-84	ME1-ME0-ME1	reverse to normal	ME1	**<1.0**		
	cpx22	c-m	88-84	ME0-ME1	reverse to normal	ME1	**<1.7**		

represent upper limits of residence times in a magmatic environment, mostly in ME2 (Table 3). The timescales modelled using Method II are residence times themselves, ranging from 9 to 32 years, and again mostly concerning ME2 (Table 3). Crystals belonging to the different analysed samples yield similar estimates. The uncertainties of time determinations were calculated for Method II propagating the uncertainties in the determination of temperature; thus maximum and minimum errors were calculated for each value based on the standard error of estimates of the thermometer (18.2 °C; Masotta et al., 2013). This allows to account also for the small differences in the temperature values obtained with the two thermometers.

5. Discussion

5.1. Crystal-melt evolution in the 79 CE feeding system

We compare and discuss MELTS modelling results with the geothermometric models, literature data and experimental studies to: (i) describe the melt-crystal evolution of a nearly primitive

magma up to the shallow storage regions of Vesuvius and (ii) obtain further constraints on the magma storage conditions. Primitive eruptive products are almost lacking at Somma-Vesuvius. Rare evidences of primitive magmas feeding the Somma-Vesuvius plumbing system were found in melt inclusions from the Avellino eruption (4.36 ka) and from recent activity (1906 and 1944 eruptions; Marianelli et al., 1995; Esposito et al., 2023) although their crystallisation conditions are not well defined. Esposito et al. (2023) highlighted that volatile-rich melt inclusions in Fo-rich olivine from the 79 CE eruption were trapped at a pressure of approximately 4–5 kbar, corresponding to a depth of ~13–16 km, which is very close to the estimated Moho depth (17.5 km; Nunziata et al., 2006). Similar high pressures were recorded by melt inclusions within olivine crystals erupted during the 1794–1944 CE Vesuvius eruptions (Marianelli et al., 1999,2005). According to the general picture presented above, we applied MELTS modelling to constrain the pre-eruptive conditions of the 79 CE magmas.

5.1.1. ME0-ME1: The mafic magma

For beginning we modelled the evolution of a primitive magma (i.e. a basalt to trachy-basalt with Mg# = 71 and CaO/Al_2O_3 = 1.18) that, whilst migrating from its mantle source, undergoes a progressive decrease in pressure and temperature (Supplementary Data Table S7). At pressures of 4.5–4 kbar, while temperature decreases from ~1200 °C to 1120 °C, the Mg# and CaO/Al_2O_3 of the melt vary from 70 to 60 and from 1.12 to 0.71, respectively (Fig. 6b and c; Supplementary Data Table S7). Such melt compositions (Mg# = 70–60) are well represented by melt inclusions in diopsidic clinopyroxene and Fo-rich olivine (Esposito et al., 2023). At these *X-P-T* conditions, the evolution of melt is driven by the crystallisation of clinopyroxene and olivine (Fig. 6c). Experimental phase equilibria (Pichavant et al., 2014), mineral-melt equilibrium and thermodynamic modelling (Figs. 5 and 6; Supplementary Data Tables S7 and S9), all indicate that, for the aforementioned range of melt compositions, the Mg# in clinopyroxene varies from approximately 91 to 80 that corresponds to the compositional populations ME0 (Mg# = 87–92) and ME1 (Mg# = 82–86) (Fig. 3). Therefore, magmatic environments ME0 and ME1 may correspond to slightly compositionally different (trachy-basalt and K-tephrite) primitive mafic batches.

5.1.2. ME2: The compositionally intermediate magma

MELTS modelling shows that, in the pressure range of 4–3.5 kbar, when temperature decreases from ~1120 to 1080 °C, the primitive magma evolves into a phono-tephrite. Phono-tephritic compositions are represented only in a few melt inclusions, found in olivine with composition Fo_{73-76} (Esposito et al., 2023). At lower pressures (3.5–2.5 kbar), when temperature decreases till 950 °C, the magma reaches a tephri-phonolitic composition (Fig. 6a) which is represented by the 79 CE whole rocks and groundmass glass composition, mainly those of the grey pumices. Therefore, in this temperature range (~1120–950 °C), the melt evolves and its Mg# ranges from 60 to 30 (Fig. 6b and c). The ME2 clinopyroxenes (Mg# = 81–64; Fig. 5a) are in equilibrium with the latter melts, whilst olivine, according to the MELTS results, have Fo_{60-80} compositions. Therefore, the *P-T* conditions at 3.5–2.5 kbar and 1120–950 °C represent a magmatic environment where a phono-tephritic magma forms, is stored and partially evolves at its shallowest levels to tephri-phonolite.

5.1.3. ME3-ME4: The evolved magma

At pressures of 2.5 kbar, with temperature ranging from ~950 to 840 °C, the composition of melt evolves from Mg# = 30 to < 30, reaching the phonolitic composition of the white pumices (Fig. 6). Clinopyroxenes crystallising in equilibrium with tephri-phonolitic and phonolitic melts belong to the ME3 and ME4 compositional populations, with crystallisation temperatures of 950–920 °C and 890–860 °C (Fig. 5; Fig. 6d), respectively. These findings are in agreement with the experimental results on the 79 CE phonolites (Scaillet et al., 2008).

5.1.4. Further constraints from MELTS modelling

Our MELTS modelling, in agreement with the different geothermometer calculations (Fig. 6d; Masotta et al., 2013; Bardeglinu et al., 2020) and the experimental results (Scaillet et al., 2008; Pichavant et al., 2014), proves the relationship between the less and more evolved products of the 79 CE eruption. The evolution from trachy-basalt to tephri-phonolite was reproduced with equilibrium crystallisation experiments at 1–2 kbar by Pichavant et al. (2014), while the crystallisation conditions of the 79 CE phonolites were experimentally constrained at 2 kbar by Scaillet et al. (2008). The reason for the discrepancy in crystallisation pressures determined through experiments and those simulated by MELTS modelling remains unclear at this time. However, considering the constraints derived from recent studies on melt inclusions (Esposito et al., 2023), MELTS modelling has demonstrated the capacity to reproduce the compositions of liquids and mineral phases undergoing a progressive decrease in pressure and temperature, as well as variations in oxygen fugacity. Further constraints can be gained from the crystallisation conditions of the main mineral phases.

Olivine – The composition of olivine and its role in the evolution of the Vesuvius magmas represents another point of interest due to (i) its rare presence in the eruptive products (Santacroce et al., 1993; Cioni et al., 1995) and (ii) the difficulties to experimentally constrain its occurrence (Trigila and De Benedetti, 1993; Pichavant et al., 2014). MELTS modelling constrains the crystallisation of olivine ($Fo_{60-89.5}$) during melt evolution when Mg# and CaO/Al_2O_3 decrease from 71.7 to 45.0 and from 1.17 to 0.43, respectively, reproducing the two compositional groups of olivine along with their melt inclusion chemistry. This supports the role of olivine in the early stages of magma differentiation. The scarcity of olivine in erupted products may partially reflect resorption driven by carbonate assimilation, as suggested by previous experimental studies (Iacono-Marziano et al., 2009; Pichavant et al., 2014).

Phlogopite – MELTS modelling (Fig. 6c) shows that at temperatures of ~1000 °C and at melt's Mg# < 50, the mineral assemblage of the tephri-phonolite is characterized by the disappearance of olivine and the stability of phlogopite, which is in agreement with experimental results (Pichavant et al., 2014). Phlogopite characterises both the white and grey pumices, and its Mg# varies from 71 to 82 — the highest values being found in phlogopite crystals from the grey pumices and from magmatic cumulates (Cioni et al., 1995).

Alkali Feldspar – Alkali feldspar is ubiquitous in the mineral assemblage of the tephri-phonolitc (grey) and phonolitic (white) pumices. MELTS modelling and experimental results concord that alkali feldspar becomes stable at $T \leq 900$ °C in the evolved tephri-phonolitc to phonolitic magma(s), which are in equilibrium with the ME3-ME4 clinopyroxenes.

5.2. Evidence from light noble gases and C isotopes in fluid inclusions

The $^3He/^4He$ ratios of the present-day Vesuvius gas emissions are comparable with those of fluid inclusions in minerals from Plinian and inter-Plinian tephra and lavas, including those of 79 CE eruption (Allard et al., 1983; Tedesco et al., 1990; Graham et al., 1993; Graham and Lupton, 1999; Martelli et al., 2004; Gherardi et al., 2022). The most magmatic samples typically show $^3He/^4He$ ratios in the narrow range of 2.6–2.8 Ra. In contrast, helium iso-

topic ratios < 2 Ra are generally observed in some spring gases (Federico et al., 2002) and in leucite and sanidine minerals from erupted products (Gherardi et al., 2022), suggesting shallow contamination by radiogenic ^{4}He from U-Th-rich rocks, or helium loss from crystals through diffusion. Helium isotope data, here obtained from olivine and clinopyroxene crystals in mafic cumulates, as well as clinopyroxene from grey pumices, show a remarkably consistent ^{3}He/^{4}He compositions ranging from 2.6 to 2.7 Ra (Supplementary Data Table S5). This range aligns closely with the most magmatic values from previous studies. We observed that clinopyroxenes from grey pumice exhibit a ^{40}Ar/^{36}Ar ratio of 295.7, closely matching the atmospheric signature, whereas cumulates VT-C1 and VT-C2 display average ratios of 319 and 301, respectively, indicating slightly less contamination by atmosphere-derived fluids and a highly deep provenance. Generally, the ^{40}Ar/^{36}Ar compositions measured in Vesuvius fluid inclusions fall within the range expected for subduction-related volcanism (Lages et al., 2021; Rizzo et al., 2021), where contamination from recycled atmosphere-derived fluids likely occurs within the mantle itself.

Fluids from the magmatic source sustain the present day gas emissions, although carbonate assimilation at shallower depths affects the carbon isotopic composition of CO_2 (Federico et al., 2002; Gherardi et al., 2022). It is generally understood that limestone contamination or assimilation occurs at mid-crustal depths at Vesuvius (Iacono-Marziano et al., 2007, 2009; Pichavant et al., 2014). However, a major question remains on whether carbonate-derived CO_2 contamination originates in the mantle from subducting sediments (Gennaro et al., 2017), within crustal carbonates, or both. Determining the depths at which melts degas and feed volcanic gases, as well as the CO_2 entrapment depth in fluid inclusions, poses a significant challenge at Vesuvius. Additionally, the extent of magma degassing in the analysed fluids can significantly alter δ^{13}C values in CO_2 trapped within magmatic crystals and in volcanic emissions, progressively lowering δ^{13}C as degassing and differentiation progress (Hoefs, 2015; Aubaud, 2022).

Our unique measurement of CO_2 trapped in clinopyroxene crystals from the VT-C1 cumulate shows a δ^{13}C of –3.8‰ and a $CO_2/^3$He ratio of 3.3×10^9 (Fig. 7). The δ^{13}C and $CO_2/^3$He values are significantly lower than those previously observed in volcanic gases ($-0.7‰ < \delta^{13}C < 0.7‰$ and $CO_2/^3He \sim 6 \times 10^{10}$; Allard et al., 1983; Chiodini et al., 2001; Federico et al., 2002; Caliro et al., 2011) and metasomatized carbonate rocks, marble and syenite xenoliths erupted during the 79 CE ($-0.5‰ < \delta^{13}C < 2.1‰$; Allard et al., 1983; Federico et al., 2002; Fulignati et al., 2005; Gherardi et al., 2022) indicating that they cannot be directly attributed to shallow carbonate contamination.

When plotting the available data in a δ^{13}C vs $CO_2/^3$He diagram (Fig. 7), we interpret that our cumulate sample results from degassing-induced fractionation of a pristine magmatic source having a gas phase with $\delta^{13}C \sim 0‰$ and $CO_2/^3He \sim 2 \times 10^{10}$ (purple line), which likely results from mixing between a MORB-like carbon and limestone, as observed in other Mediterranean subduction-related volcanism (e.g., Santorini and Vulcano; Fig. 7). Instead, volcanic gases from Vesuvius fumaroles, as well as those from Solfatara (Phlegrean Fields) (Allard et al., 1983; Chiodini et al., 2001; Federico et al., 2002; Caliro et al., 2011), whose fluids sustain the present day gas emissions, show δ^{13}C and $CO_2/^3$He values that are not representative of the pristine magmatic source. They show a significantly higher $CO_2/^3$He ratio that contrasts with the expected ratio reduction in more degassed and shallow melts (Gennaro et al., 2017; Lo Forte et al., 2024; Sandoval-Velasquez et al., 2024). These features likely reflect the addition of CO_2—released by local decarbonation of the limestone- platform—to a gas phase compositionally similar to that found in fluid inclusions from the cumulates, which had already undergone a level of degassing comparable to that recorded in our cumulate sample (red line in Fig. 7).

In this scenario, the volcanic gases emitted nowadays at Vesuvius are degassed from already differentiated and degassed melts, possibly residing at depths shallower than 10 km, i.e. within the carbonate platform, where CO_2 contamination through decarbonation is likely. Within this framework, δ^{13}C values measured in sanidine crystals, which are thought to result from decarbonation of carbonates, metalimestones, or metadolostones (Gherardi et al., 2022), would have crystallised at shallowest depths within or above the carbonate platform.

5.3. The 79 CE plumbing system architecture

Civetta and Santacroce (1992) and Santacroce et al. (1993) proposed a steady-state mafic magma supply during the last 3400 years of Somma-Vesuvius activity, and the input of mafic magma was considered responsible for the growing process of Somma-Vesuvius shallow reservoir(s). This scenario, which includes the repeated injections of deeper and mafic magma (e.g., the mafic batches of Cioni et al., 1995), is also consistent with the observed chemical zoning patterns in the clinopyroxene crystals. The different compositional populations (MEs) reflect different P-T conditions and melt compositions. Their abundances and the relations among them, detected through the zoning patterns, yield information on the sequence of events that occurred pre-eruptively in the 79 CE plumbing system. Most of the analysed clinopyroxenes (~75%) are representative of the magmatic environments ME0 and ME2. The abundant normally zoned profiles are dominated by crystal cores with the composition ME0 (Mg# = 87–92) and rims with the composition ME2 (Mg# = 64–81) (Fig. 4). Reverse zoning pattern characterizes only 26% of the analysed profiles, with some (9%) of them presenting cores with ME3 composition (Mg# = 50–62) and rims with ME2 composition. For both normally and reversely zoned profiles, ME2 constitutes the rim composition in 71% of the crystals (Figs. 3 and 4), hence, representing the last crystallising environment experienced by most of the clinopyroxenes. Primitive magmas (trachy-basalts to K-tephrites) are injected in the deep crust, crystallising and segregating Fo-rich olivine and ME0-ME1 clinopyroxene to form cumulates (i.e., VT-C1, VT-C2). Clinopyroxenes with composition ME0, whose crystallisation temperature is ~1200–1120 °C (Fig. 5), were possibly transported by the periodic rise of mafic batches in a phono-tephritic reservoir at temperature of ~1000 °C where normally zoned crystals (ME0 cores to ME2 rims) form. Oscillations between ME0, ME1 and ME2 (e.g., red lines in Fig. 4) suggest long lasting connectivity between mafic batches, cumulates, and the phono-tephritic magma. The ME0 clinopyroxenes could be either phenocrysts of trachy-basaltic to K-tephritic magmas or cumulate antecrysts remobilized by the deeper batches. On this basis, it is reasonable to interpret that ME2 is the physical environment where most of the magmatic interaction(s) took place: it can represent the first thermal and density barrier to the entry of the denser and hotter mafic magma batches. The hypothesized recharge scenario and consequent mixing is also supported by both the texture of most zoned crystals, which show resorbed and patchy zoned cores (Supplementary Data Fig. S5), and by the Sr-isotopic signature. Feldspars that are separated from the white pumice are in isotopic equilibrium with their host rocks (^{87}Sr/^{86}Sr = 0.7077; Supplementary Data Fig. S2b). This suggests that alkali feldspars and ME3 and ME4 clinopyroxenes from the phonolitic portion (white pumices) of the reservoir approached crystal–liquid equilibrium before eruption. In contrast, feldspars that are separated from the grey pumice (^{87}Sr/^{86}Sr = 0.70767–0.70769) have Sr isotopic ratios similar to the white pumice, hence they grew in the phonolite and were subsequently remobilized in the tephri-phonolitic

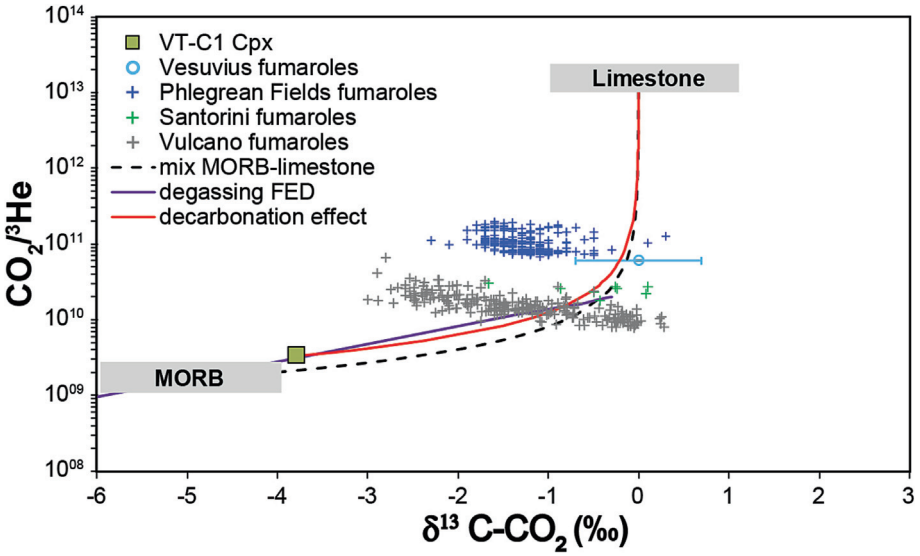

Fig. 7. $CO_2/^3He$ vs $\delta^{13}C$ in clinopyroxene-hosted fluid inclusions from the VT-C1 cumulate compared to literature data. Literature data from: (i) average value of Vesuvius crater fumarole (Chiodini et al., 2001); (ii) Solfatara (Phlegrean Fields; Caliro et al., 2011); (iii) Vulcano fumaroles (Aeolian Islands; Paonita et al., 2013); (iv) Santorini fumaroles (Aegean Volcanic Arc; Rizzo et al., 2016). The black dotted line represents the mixing between a MORB-like carbon ($-6‰ < \delta^{13}C < -4‰$ and $CO_2/^3He \sim 2 \times 10^9$; Marty and Jambon, 1987; Javoy and Pineau, 1991) and limestone ($-1‰ < \delta^{13}C < 1‰$ and $CO_2/^3He \sim 1 \times 10^{13}$; Sano and Marty, 1995). The purple line indicates an open system degassing path (Fractional Equilibrium Degassing; equation of Jambon et al., 1986; Macpherson and Mattey, 1994; Hoefs, 2015), while the red line a mixing between a magmatic term with a composition like that of our cumulate sample and a limestone, intended as a progressive addition of carbon from decarbonation of the carbonate platform. Starting conditions for degassing modelling of the gaseous phase are: $\delta^{13}C = -0.3‰$ and $CO_2/^3He = 2 \times 10^{10}$, εvap-melt = 2.7‰ (Mattey, 1991), SHe = 2.3×10^{-4} cm^3 STP g^{-1} bar^{-1}, $SCO_2 = 1 \times 10^{-4}$ cm^3 STP g^{-1} bar^{-1} (Gennaro et al., 2017).

magma (grey pumices). Clinopyroxenes ($^{87}Sr/^{86}Sr$ = 0.70717–0.70737) have isotopic ratios lower than the grey host pumice. Their Sr-isotopic signature can be tentatively associated with the clinopyroxene compositional populations ME1 and ME0, and hence with the trachy-basalt and K-tephrite.

The magmatic environment ME2, hence, corresponds to a set of conditions where a phono-tephritic to tephri-phonolitic magma, located below the phonolitic reservoir (ME3-ME4), interacts with mafic batches and their crystal cargo represented by ME0-ME1. Assuming that the phonolitic reservoir of the 79 CE eruption was emplaced at ~7.5 km depth (Balcone-Boissard et al., 2008,2011), and that it had a small vertical extent, we propose that a further mafic reservoir may have existed below 8 km. This hypothesis is consistent with the existence of a vertically extended magmatic system, and is compatible with the model of reservoir growth and ground deformation prior to the 79 CE eruption (Doronzo et al., 2023).

Several geochemical and geophysical studies have estimated the carbonate platform beneath Vesuvius to extend to around 12 km depth (Belkin et al., 1998; Fulignati et al., 2004; Nunziata et al., 2006; Esposito et al., 2023). A schematic sketch of the Somma-Vesuvius magmatic system is presented in Fig. 8, including the link among the recognized MEs, as displayed by the zoning patterns.

MELTS modelling suggests that olivine and clinopyroxene crystals in mafic cumulates likely crystallised from a primitive trachy-basaltic magma at pressures of 5–4.5 kbar, while clinopyroxenes from grey pumice probably formed in phono-tephritic to tephri-phonolitic magmas at pressures of 4–2.5 kbar. If this depth is accurate, our $\delta^{13}C$ value of –3.8‰ supports the MELTS model by suggesting that cumulate crystals crystallised below the carbonate platform, avoiding CO_2 contamination by intra-crustal decarbonation (Fig. 7).

The grey-white magma transition was discussed in depth by Cioni et al. (1995). The authors suggest a sharp compositional break between tephri-phonolite and phonolite magmas within the chamber and a complete mixing process occurring when the residual liquid from the crystallisation of grey magma reached a density equal to that of the white layer. These mechanisms also efficiently explain the rare reverse zoning patterns (ME3 cores to ME2 rims) observed in the 79 CE clinopyroxene (Fig. 4), as well as the few normal zoning patterns from ME2 cores and mantles to ME3 rims. The preservation of zoning patterns confirms that crystals were incorporated in the erupted magma not long before the beginning of the eruption. Indeed, the time estimated from the mixing to a near complete hybridization was less than 15 h (Cioni et al., 1995). This refers to the *syn*-eruptive physical mixing (mingling) of melts occurring in the last moments just before the eruption, whereas crystals record the previous history of older processes (e.g., Pelullo et al., 2024).

5.4. Timescales of magmatic processes before the 79 CE eruption

The differentiation processes and the formation of the plumbing system architecture are expected to take place over long timescales (e.g., hundreds to thousands of years). For the phonolitic magma of the 79 CE eruption, garnet uranium–thorium petrochronology suggests storage in the upper crust of ~1 ka (Wotzlaw et al., 2022).

Morgan et al. (2006) applied Ba diffusion modelling to sanidine crystals of the 79 CE eruption to obtain time estimates. The sanidine showed resorption/regrowth evidence and the authors related the chemical variations in the crystal profiles to three distinct recharge events that occurred in the century before the eruption. Overall, their timescales, calculated at 870 °C, range from 84 to 16 years, with most values being <35 years. Moreover, they statistically calculated a peak at ~20 years for the last recharge event. Our MELTS modelling underscores the beginning of feldspar crystallisation at slightly higher temperatures (880 °C) and within a ±20 °C range. This can affect diffusion time estimates by one order of magnitude, and as such, if performed at slightly higher temperatures, the timescales calculated by Morgan et al. (2006) would be in the same range as our times estimates. With respect to previous works, our diffusion modelling calculations indicate

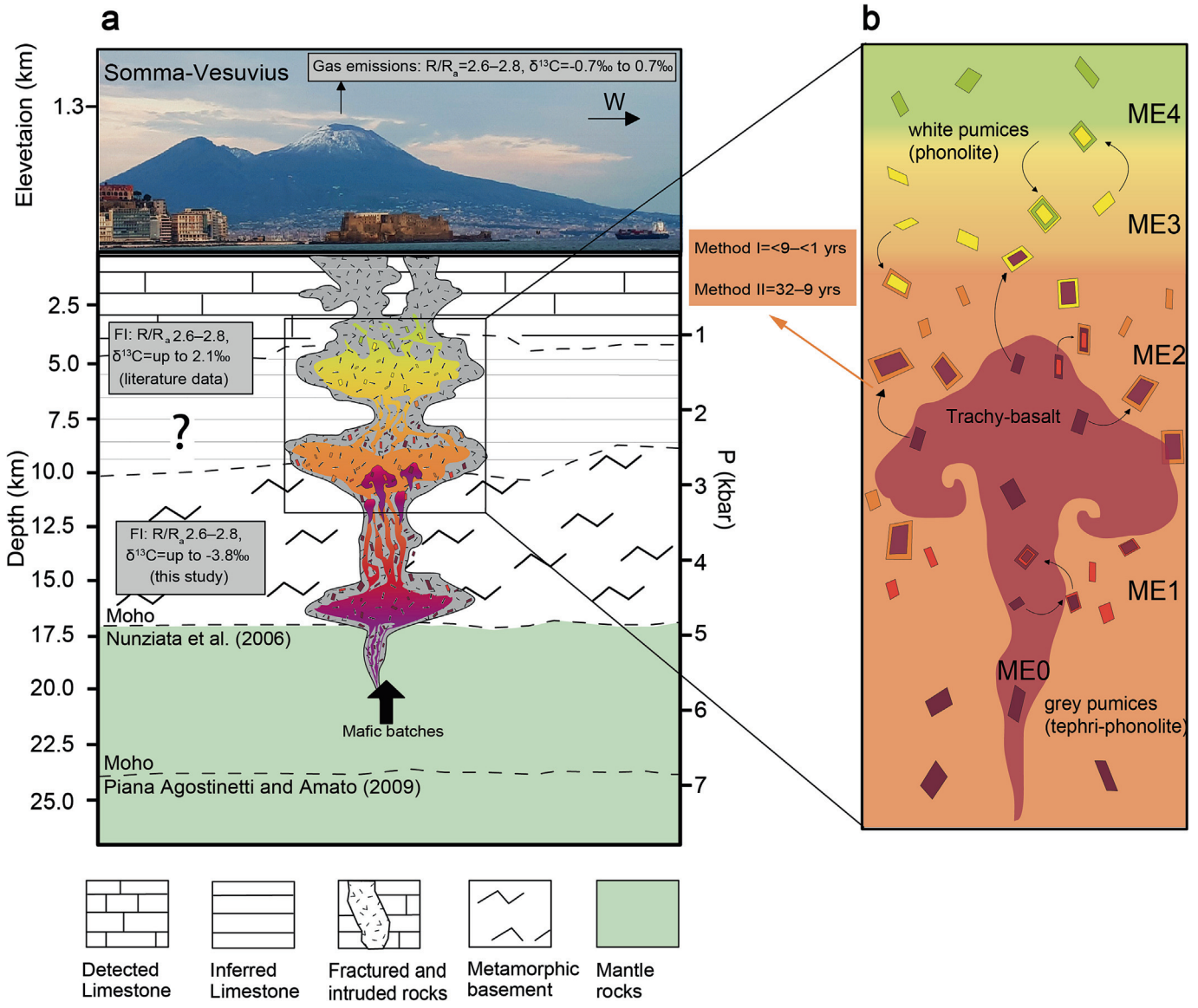

Fig. 8. The 79 CE plumbing system architecture, the pre-eruptive dynamics and their timescales based on the whole geochemical data and modelling. (a) Geological schematic cross section of Somma-Vesuvius modified from the literature (Nunziata et al., 2006; Esposito et al., 2023). Two inferred Moho depths (Nunziata et al., 2006; Piana Agostinetti and Amato, 2009) are shown while the question mark is related to the uncertainty of the carbonate platform depth (6 or 12 km). The fractured and intruded rocks were extended according to MELTS modelling. Noble gas and carbon isotopes of gas emissions and fluid inclusions (FI) from literature data (Chiodini et al., 2001; Federico et al., 2002; Martelli et al., 2004; Gherardi et al., 2022) are also reported. (b) The plumbing systems of the 79 CE eruption in terms of the five distinct MEs detected from the clinopyroxene zoning pattern. Repeated input of ME0 mix with ME2 leading to the formation of the chemically intermediate long-lasting phono-tephritic to tephri-phonolitic reservoir.

crystal residence durations mostly at the ME2 conditions (Table 3). In particular, Method I allowed to constrain the upper time limit that 18 crystals may have spent in a certain magmatic environment, corresponding to less than 10 years (with 11 out of 18 being less than 5 years). In contrast, Method II indicate residence times between 9 and 32 years, for other 7 crystals. The different times obtained can hence be related to the different episodes of crystal transfer mostly from the ME0 to the ME2 environment. The differences in the clinopyroxene compositions possibly record the different moments at which the crystals resided at the *X-P-T* condition of ME2. In fact, the behaviors of different elements (Fe-Mg, Al) in the clinopyroxenes (Fig. 2) suggest that some zoned crystals (those modelled with Method II), showing more evidence of diffusion, could have been transferred to the ME2 environment before those that were less affected (or not at all and modelled with Method I) by diffusion. These differences may well reflect the different times of crystals transfer, thus highlighting the repeated occurrence of the mafic recharge. Magma recharge events did not build up immediate critical conditions to rapidly trigger the eruption; on the contrary, magma resided for years in the ME2 reservoir. Timescales of magma injection in the range of years to centuries have been estimated for other Plinian eruptions by Weber et al. (2019), which highlighted a recurrent recharging pattern prior to the eruptions. The hypothesis of recharging events causing the growth of the 79 CE feeding system was explored by Doronzo et al. (2023). The authors emphasize the role of magma recharge processes, assuming that multiple episodes of magma injection contributed to the reservoir's growth over a 300-year period. For simplicity, they adopted a fixed frequency of magma recharge of 60 years, which can be refined here by the diffusion modelling, indicating a shorter timespan elapsed among the recharge events, at least for those that occurred in the periods close to the eruption.

5.5. Timescales of magmatic processes and seismicity in the I century CE: Are they linked?

Volcanic eruptions occur when magma ascends through the crust to the Earth's surface and are, usually, preceded by signs of unrest, such as seismicity, ground deformation and gas emissions (e.g. Sigmundsson et al., 2018; Caricchi et al., 2021; Martí, 2024).

The duration of the unrest phase can provide fundamental information on the dynamics of magma ascent from the magma reservoir, until building up critical conditions (e.g., Passarelli and Brodsky, 2012; Caricchi et al., 2021; Martí, 2024). Several recent studies (Saunders et al., 2012; Martí et al., 2013; Shapiro et al., 2017; Ostorero et al., 2022) have correlated seismic activity with plumbing system processes (e.g., magma mixing, reservoir recharge, fluid pressure propagation) preceding and triggering eruptions.

For historical eruptions that occurred before the era of monitoring instruments, the historical chronicles reporting the occurrence of seismic activity (or any other potentially precursor phenomenon) months to years in advance of (large) eruptive events are of paramount importance. The integration of seismicity with the investigation of timescales of magmatic processes, eventually triggering volcanic activity, has implications for risk mitigation (e.g. Zanon et al., 2022, 2024; Ostorero et al., 2025).

Prior to the 79 CE eruption, at least three historically ascertained earthquakes occurred in 37, 62 and 64 CE (e.g. Cubellis and Marturano 2002, 2013; Marturano, 2008) (Fig. 9).

In addition to these documented earthquakes, the occurrence of seismic events between 64 and 79 CE has been hypothesized through the integration of vague historical information and archaeological data (e.g. Marturano, 2006, 2008), with a relevant seismic period bracketed between 72 and 78 CE and in the year/months before the eruption (Marturano, 2006, 2008). Moreover, tremors were clearly felt for several days before the eruption according to Pliny the Younger's second letter to Tacitus (*Epistulae*, VI.20).

Notably, the timescales derived from Fe-Mg diffusion modelling overlap with the chronology of the earthquakes that plagued the Vesuvius territory (Fig. 9). The 62 and 64 CE events and, when considering the uncertainties, the 37 CE earthquake, are well consistent with the timescales yielded by Method II. The inferred seismicity that occurred after the 64 CE earthquake until the 72 CE is consistent with some estimates obtained with Method II and some of those obtained with Method I. The relevant seismic period from the 72 CE until the eruption aligns with the estimates obtained with Method I (Fig. 9). Our diffusion timescales indicate that important variations occurred in the plumbing system (ME2) in a period between ~30 years (even 48 years, considering the uncertainties) to a few years (even less than 2 years) before the 79 CE eruption. Magma replenishment may have built up overpressure, causing fracturing of the host rock and seismicity (e.g., Currenti and Williams, 2014; Sigmundsson et al., 2018; Segall, 2019; Cas et al., 2024). On the other hand, tectonic earthquakes can perturb magmatic systems and trigger eruptions, even years or decades after their occurrence, provided that magma is reaching near critical conditions and seismic sources are in the vicinity of the volcano (e.g., Latter, 1971; Marzocchi, 2002; Walter and Amelung, 2007; Watt et al., 2009; De la Cruz-Reyna et al., 2010; Bebbington and Marzocchi, 2011; Nishimura, 2017; González et al., 2021; Legrand, 2022). At Vesuvius, several studies suggest statistical and mechanical links between the spatially close Apennine chain seismicity and major eruptions (Marzocchi et al., 1993; Nostro et al., 1998; Bragato, 2015, 2017). Whatever the origin of the documented earthquakes, magmatic (i.e. due to magma transfer) or tectonic (i.e. due to the dynamics of the Apennine), the cross-referencing of the timescales of pre-eruptive magmatic processes involved in the assembly of magmas that fed the 79 CE eruption and the historical seismicity of the I century CE supports the hypothesis of a causal link between them. In this regard, the origin (volcanic or tectonic) of the 62 CE earthquake remains under debate (e.g., Sigurdsson et al., 1985; Marturano and Rinalsis, 1998; Dal Maso et al., 1999; Marturano 2008; Galli, 2020), as it is the strongest historical seismic event occurred in the Vesuvius area (e.g., Cubellis et al., 2007). Based on the above-mentioned premises, a hypothetical tectonic origin for the 62 CE earthquake would not preclude a causal link to the 79 CE eruption. In fact, our diffusion timescales (Method II) suggest a magma recharge event in the ME2 reservoir (Table 3) in a time span compatible with the occurrence of the 62 CE earthquake. Similarly, Morgan et al. (2006) suggest a significant magma recharge about two decades before the eruption, consistent with the 62 CE earthquake. The earthquake may have been able to destabilize deep magma (e.g., from the ME0 reservoir), promoting its upward transfer and subsequent stalling in ME2, as recorded by the most common zoning (Fig. 4) and constrained by diffusion modelling (Table 3), without reaching the surface (as the magma was still not in a critical state). Magma upward migration (e.g., transfer from ME0 to ME2) may have enhanced surface degassing, consistent with Seneca's report (*Naturales Questiones*, VI.1.1-3) of the death (plausibly due to asphyxiation) of a flock of six hundred sheep at the time of the earthquake (Guidoboni, 1989). Nevertheless, taking into account that the 62 CE earthquake represents the beginning of a prolonged seismic period induced by episodes of magma transfer, as recorded by the crystal zoning and related diffusion modelling (Fig. 4; Table 3), this major seismic event could be associated with the effects produced by magmatic processes that created the conditions for the explosive awakening of Vesuvius in 79 CE. This conclusion supports an origin related to the dynamics of the volcano, as proposed by most scholars, thereby making a tectonic origin unlikely.

5.6. Hazard implications at Vesuvius

The 79 CE eruption is not the only large historical eruption of Somma-Vesuvius preceded by decade-long seismicity. The 1631 CE sub-Plinian eruption occurred after a period of sealed conduit conditions and dormancy possibly lasting not less than ~150 years (Cioni et al., 2008; Santacroce et al., 2008) although the occurrence of minor eruptive activity in the second half of XVI century has been suggested (Giudicepietro et al., 2025). Seventeen earthquakes occurred in the 15 years preceding the event, between 1616 and 1630 CE, which can represent long-term precursory phenomena (Guidoboni and Mariotti, 2011). Short-term precursory seismicity occurred in the weeks prior to the event, dramatically escalating the night before (e.g., Rosi et al., 1993; Bertagnini et al., 2006; Guidoboni and Mariotti, 2011).

In a broad view, the investigation of timescales of magmatic processes can be useful to understand how the magmatic system has behaved in the past and can behave in the future (e.g., Pelullo et al., 2024). When integrated with historical accounts of potential precursory phenomena, if available (e.g., the 1631 CE eruption), such timescales can offer valuable insights into the occurrence of unrest signals preceding an eruption, which can be detected by surveillance networks, in turn having implication on hazard assessment. Unrest episodes (months to years in advance of an eruption) at Somma-Vesuvius can be characterized by magma accumulation in a deep reservoir followed by progressive transfer to shallower segments of the plumbing system (e.g., Fig. 8). Magma migration can be associated with a progressive increase of seismicity (besides other signals) induced by the pressurization of the plumbing system (Rosi et al., 2022). The unrest signals usually intensify as the eruption approaches (weeks to months). In this regard, a hazard-related implication of our study

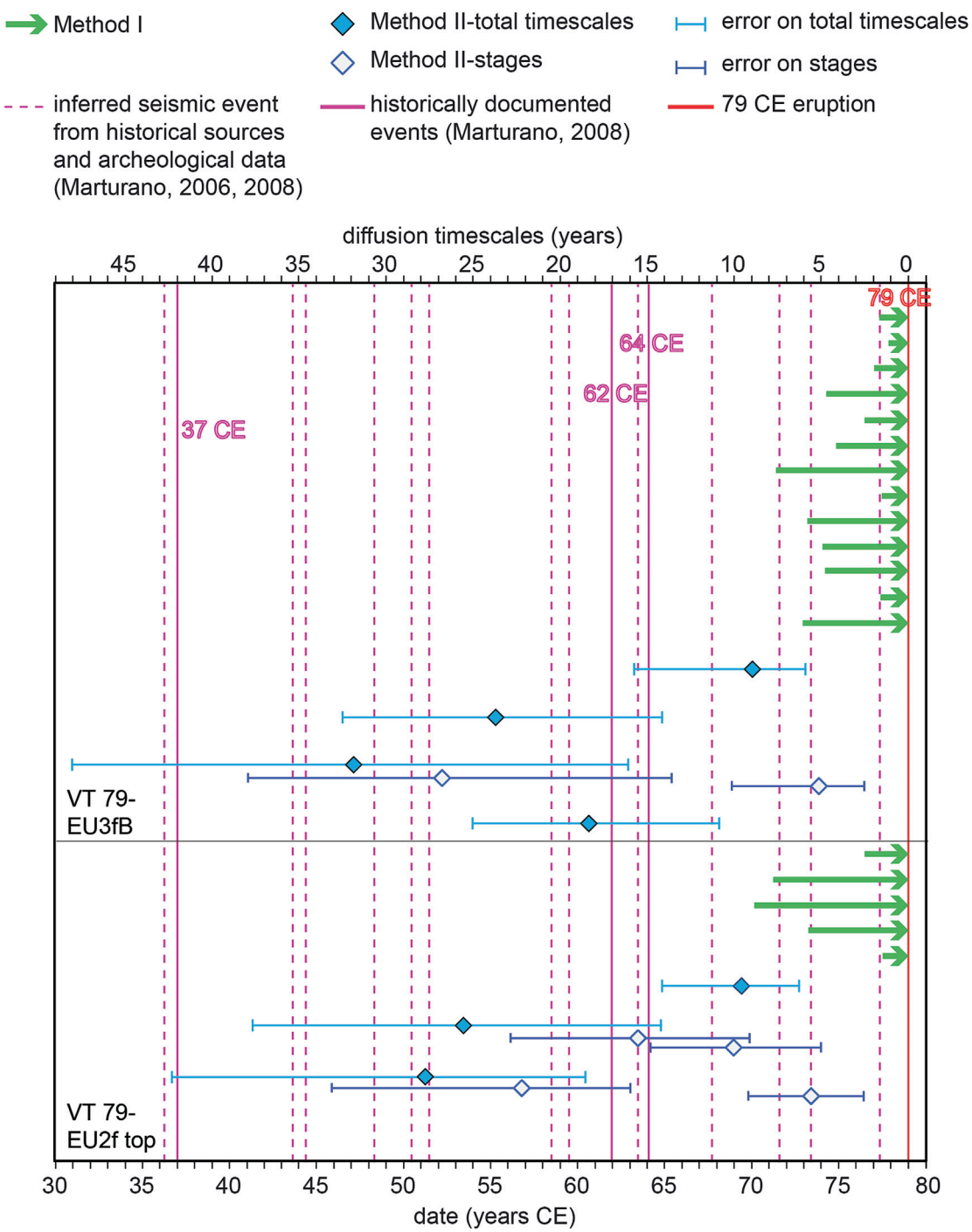

Fig. 9. Comparison between the timescales obtained through diffusion modelling and the occurrence (date) of earthquakes in the I century CE, prior to the 79 CE eruption. The green arrows represent the timescale limits set by Method I on clinopyroxenes from the eruptive products. These show enhanced magma input about 10 years before the eruption. Blue symbols with error bars represent timescales obtained using Method II on clinopyroxenes. Solid symbols represent total timescales while open symbols represent the stages from the same crystals, as reported in Table 3. Vertical purple lines represent the documented (solid lines; Marturano, 2006, 2008) and inferred (dashed lines; Marturano, 2008) earthquakes that occurred in the four decades before the eruption (red line). The results show that the timescales obtained with both Method II and Method I coincide with the recurrent seismic activity in the region.

is whether long-term (years to decades) seismicity at Somma-Vesuvius should (or not) be regarded as a potential unrest signal that may culminate in a large (Plinian and sub-Plinian) eruption. In light of this, it is interesting to note that the diffusion timescales associated with episodes of magma upward transfer prior to the 3.9 ka Avellino Plinian eruption of Somma-Vesuvius yielded values in a range of decades (15–56 years) (Falasconi et al., 2025). Based on these premises, a question arises: Was the Avellino Plinian eruption heralded by long-term (decades) seismic unrest? Unfortunately, it will remain unanswered.

Somma-Vesuvius has been experiencing sealed conduit conditions since 1944, year of the last eruption, when the volcano entered a dormant state. The length of current dormancy (over 80 years) is much longer that the duration of repose time between eruptions (mainly weak- to mild-explosive to effusive) of the last eruptive period (1631–1944), but still shorter than those that pre-

ceded Plinian and major sub-Plinian eruptions throughout the history of the volcano (Cioni et al., 2008; Scandone et al., 2008; Scandone and Giacomelli, 2008). It is impossible to establish *a priori* the duration of the repose time required to build up critical conditions leading to the occurrence of unrest signals and, possibly, culminating in an eruption. Our study suggests that the investigation of timescales of magmatic processes at Somma-Vesuvius can be an additional tool to "predict" the possible behaviour of the volcano in the years to decades prior to the renewal of the activity, possibly heralded by long-term seismicity for large eruptions.

6. Conclusions

Historical Latin texts describe earthquakes and structural damage preceding the 79 CE eruption of Vesuvius, often interpreted as divine wrath. In light of the contemporary knowledge of the unrest dynamics, these records raise critical questions: Could the residents of Pompeii have foreseen the disaster? Considering our results and current knowledge, as well as the dense geophysical and geochemical monitoring network and the role of civil protection authorities, should phenomena such as unrest, deformation, increased degassing or seismicity occur in the present or near future, can we reasonably assume that effective mitigation strategies would prevent an event comparable to the 79 CE eruption? This study provides a detailed reconstruction of the magmatic processes beneath Vesuvius leading up to the 79 CE Plinian eruption. Geochemical data and modelling indicate the presence of a vertically extended magmatic system, where mafic magma ascended from deep storage to a shallower reservoir (~3.5–2 kbar) over decades, most frequently in the final years before eruption. In fact, the clinopyroxene crystals record residence for 30–20 years, while most of them for less than 10 years (mostly less than 5 years) in a phono-tephritic magma reservoir before the eruption. These findings align with the historical record of seismicity and offer a framework for understanding precursory activity in future eruptions. The study highlights the interplay between seismic activity and magma transfer, suggesting that whether magma chamber growth triggered prolonged seismicity or seismic events facilitated magma movement, the combination of these processes was responsible for the damage to inhabited areas and ultimately led to the catastrophic Plinian eruption which destroyed Pompeii and Herculaneum. Similar decades-long periods of unrest, with related seismicity, were observed for other highly explosive events (e.g., the sub-Plinian 1631 eruption) of Vesuvius. Identifying warning precursory signs and their run-up time would allow a more precise volcanic hazard assessment and integrating this knowledge with modern monitoring techniques can contribute to adequately improving the risk mitigation strategies.

CRediT authorship contribution statement

Pierangelo Romano: Writing – review & editing, Writing – original draft, Visualization, Software, Resources, Methodology, Investigation, Formal analysis, Data curation. **Carlo Pelullo:** Writing – review & editing, Writing – original draft, Visualization, Resources, Methodology, Investigation, Formal analysis, Data curation, Conceptualization. **Sumit Chakraborty:** Writing – review & editing, Validation, Supervision, Investigation, Formal analysis, Data curation, Conceptualization. **Andrea Luca Rizzo:** Writing – review & editing, Visualization, Validation, Supervision, Resources, Project administration, Methodology, Investigation, Funding acquisition, Formal analysis. **Hélène Balcone-Boissard:** Writing – review & editing, Visualization, Validation, Supervision, Resources, Investigation, Formal analysis, Data curation. **Domenico Sparice:** Writing – review & editing, Visualization, Validation, Resources, Investigation, Formal analysis. **Domenico Maria Doronzo:** Writing – review & editing, Validation, Resources, Investigation. **Mauro Antonio Di Vito:** Writing – review & editing, Supervision, Resources, Project administration, Funding acquisition. **Ilenia Arienzo:** Writing – review & editing, Validation, Supervision, Resources, Project administration, Investigation, Funding acquisition, Data curation, Conceptualization.

Declaration of competing interest

The authors declare that they have no known competing financial interests or personal relationships that could have appeared to influence the work reported in this paper.

Acknowledgements

The authors are grateful to Dr. Manuela Nazzari (INGV-Roma1) for her availability and help in the acquisition of microanalytical data. The INGV-OV laboratories have been financially supported by the EPOS Research Infrastructure through the contribution of the Italian Ministry of University and Research (MUR). This work was supported by the Istituto Nazionale di Geofisica e Vulcanologia, Italy, grant "Progetto INGV Pianeta Dinamico" - code CUP D53J19000170001 - funded by Italian Ministry MIUR ("Fondo Finalizzato al rilancio degli investimenti delle amministrazioni centrali dello Stato e allo sviluppo del Paese", legge 145/2018) - Tasks V1 (A.L.R), V3 (M.A.D.V.), and from 2023-2025, sub-project SMEEGOL (I.A.) and with the financial support of Presidenza del Consiglio dei Ministri and Dipartimento della Protezione Civile DPC-INGV project. We thank Mariano Tantillo and Mariagrazia Misseri for helping in samples preparation and CO_2 extraction from minerals, and Ygor Oliveri and Giorgio Capasso for the isotope analysis of carbon of CO_2 performed in the stable isotope laboratory of INGV, Sezione di Palermo. We are grateful to Karoly Nemeth, Tong Hou, Rafael Torres-Orozco, and an anonymous reviewer who provided constructive feedback on the manuscript, and the Associate Editor Stijn Glorie for editorial handling.

Appendix A. Supplementary data

Supplementary data to this article can be found online at https://doi.org/10.1016/j.gsf.2026.102283.

References

Allard, P., 1983. The origin of hydrogen, carbon, sulphur, nitrogen and rare gases in volcanic exhalations: evidence from isotope geochemistry. In: Tazieff, H., Sabroux, J.C. (Eds.), Forecasting Volcanic Events. Elsevier, Amsterdam, pp. 337–386.

Amstutz, F.M., Stock, M.J., Smith, V.C., Isaia, R., Vitale, S., Carter, E.J., Natale, J., 2025. Volcano-tectonic controls on magmatic evolution at Campi Flegrei, Italy: Insights from thermodynamic modelling. J. Petrol. 66, egaf068. https://doi.org/10.1093/petrology/egaf068.

Aubaud, C., 2022. Carbon stable isotope constraints on CO_2 degassing models of ridge, hotspot and arc magmas. Chem. Geol. 605, 120962. https://doi.org/10.1016/j.chemgeo.2022.120962.

Balcone-Boissard, H., Boudon, G., Cioni, R., Webster, J.D., Zdanowicz, G., Orsi, G., Civetta, L., 2016. Chlorine as a geobarometer for alkaline magmas: evidence from a systematic study of the eruptions of Mount Somma-Vesuvius. Sci. Rep. 6, 21726. https://doi.org/10.1038/srep21726.

Balcone-Boissard, H., Boudon, G., Ucciani, G., Villemant, B., Cioni, R., Civetta, L., Orsi, G., 2012. Magma degassing and eruption dynamics of the Avellino pumice Plinian eruption of Somma–Vesuvius (Italy). Comparison with the Pompeii eruption. Earth Planet. Sci. Lett. 331–332, 257–268. https://doi.org/10.1016/j.epsl.2012.03.011.

Balcone-Boissard, H., Boudon, G., Villemant, B., 2011. Textural and geochemical constraints on eruptive style of the 79 AD eruption at Vesuvius. Bull. Volcanol. 73, 279–294. https://doi.org/10.1007/s00445-010-0409-0.

Balcone-Boissard, H., Villemant, B., Boudon, G., Michel, A., 2008. Non-volatile vs volatile behaviours of halogens during the AD 79 plinian eruption of Mt.

Vesuvius, Italy. Earth Planet. Sci. Lett. 269 (1-2), 66–79. https://doi.org/10.1016/j.epsl.2008.02.003.
Barberi, F., Bizouard, H., Clocchiatti, R., Metrich, N., Santacroce, R., Sbrana, A., 1981. The somma-vesuvius magma chamber: a petrological and volcanological approach. Bull. Volcanol. 44 (3), 295–315. https://doi.org/10.1007/BF02600566.
Bardeglinu, I., Cioni, R., Scaillet, B., 2020. Experimental constraints on pre-eruption conditions of the 1631 Vesuvius eruption. J. Volcanol. Geoth. Res. 406, 107076. https://doi.org/10.1016/j.jvolgeores.2020.107076.
Baxter, P.J., Horwell, C.J., 2015. Chapter 60 - impacts of eruptions on human health. In: Sigurdsson, H. (Ed.), The Encyclopedia of Volcanoes (Second Edition). Academic Press, Amsterdam, pp. 1035–1047. https://doi.org/10.1016/B978-0-12-385938-9.00060-2.
Belkin, H.E., De Vivo, B., Török, K., Webster, J.D., 1998. Pre-eruptive volatile content, melt-inclusion chemistry, and microthermometry of interplinian Vesuvius lavas (pre-A.D. 1631). J. Volcanol. Geoth. Res. 82, 79–95. https://doi.org/10.1016/S0377-0273(97)00058-9.
Black, S., Macdonald, R., DeVivo, B., Kilburn, C.R.J., Rolandi, G., 1998. U-series disequilibria in young (A.D. 1944) Vesuvius rocks: Preliminary implications for magma residence times and volatile addition. J. Volcanol. Geoth. Res. 82, 97–111. https://doi.org/10.1016/S0377-0273(97)00059-0.
Bebbington, M.S., Marzocchi, W., 2011. Stochastic models for earthquake triggering of volcanic eruptions. J. Geophys. Res. [Solid Earth] 116, B05204. https://doi.org/10.1029/2010JB008114.
Bertagnini, A., Cioni, R., Guidoboni, E., Rosi, M., Neri, A., Boschi, E., 2006. Eruption early warning at Vesuvius: the A.D. 1631 lesson. Geophys. Res. Lett. 33, L18317. https://doi.org/10.1029/2006GL027297.
Blundy, J., Cashman, K., 2008. Petrologic reconstruction of magmatic system variables and processes. Rev. Mineral. Geochem. 69, 179–239. https://doi.org/10.2138/rmg.2008.69.6.
Bragato, P.L., 2015. Italian seismicity and Vesuvius' eruptions synchronize on a quasi 60 year oscillation. Earth Space Sci. 2 (5), 134–143. https://doi.org/10.1002/2014ea000030.
Bragato, P.L., 2017. Correlation between seismic and volcanic activity at a large spatial scale in Italy: examples from the Neapolitan Volcanic district (Vesuvius Volcano, Southern Italy). In: Aiello, G. (Ed.), Volcanoes - Geological and Geophysical Setting, Theoretical Aspects and Numerical Modeling, Applications to Industry and Their Impact on the Human Health. IntechOpen, London, pp. 19–33. https://doi.org/10.5772/intechopen.71977.
Brown, R.J., Civetta, L., Arienzo, I., D'Antonio, M., Moretti, R., Orsi, G., Tomlinson, E.L., Albert, P.G., Menzies, M.A., 2014. Geochemical and isotopic insights into the assembly, evolution and disruption of a magmatic plumbing system before and after a cataclysmic caldera-collapse eruption at Ischia volcano (Italy). Contrib. Mineral. Petrol. 168, 1035. https://doi.org/10.1007/s00410-014-1035-1.
Buono, G., Pappalardo, L., Harris, C., Edwards, B.R., Petrosino, P., 2020. Magmatic stoping during the caldera-forming Pomici di Base eruption (Somma-Vesuvius, Italy) as a fuel of eruption explosivity. Lithos 370–371, 105628. https://doi.org/10.1016/j.lithos.2020.105628.
Caliro, S., Chiodini, G., Avino, R., Minopoli, C., Bocchino, B., 2011. Long time-series of chemical and isotopic compositions of Vesuvius fumaroles: evidence for deep and shallow processes. Ann. Geophys. 54, 137–149. https://doi.org/10.4401/ag-5034.
Cannatelli, C., 2012. Understanding magma evolution at Campi Flegrei (Campania, Italy) volcanic complex using melt inclusions and phase equilibria. Min. Petrol. 104, 29–42.
Caricchi, L., Townsend, M., Rivalta, E., Namiki, A., 2021. The build-up and triggers of volcanic eruptions. Nat. Revi. Earth Environ. 2 (7), 458–476.
Cas, R., Giordano, G., Wright, J.V., 2024. Fragmentation processes in magmas and volcanic rocks: autoclastic, explosive, hydraulic fracturing—characterising clast and aggregate properties. In: Cas, R., Giordano, G., Wright, J.V. (Eds.), Volcanology: Processes, Deposits, Geology and Resources. Springer Textbooks in Earth Sciences, Geography and Environment. Springer, Cham, pp. 115–225. https://doi.org/10.1007/978-3-319-66613-6_4.
Chakraborty, S., Ganguly, J., 1991. Compositional zoning and cation diffusion in garnets. In: Ganguly, J. (Ed.), Diffusion, Atomic Ordering, and Mass Transport: Selected Topics in Geochemistry. Springer, New York, pp. 120–175. https://doi.org/10.1007/978-1-4613-9019-0_4.
Chiodini, G., Marini, L., Russo, M., 2001. Geochemical evidence for the existence of high-temperature hydrothermal brines at Vesuvio volcano, Italy. Geochim. Cosmochim. Acta. 65, 2129–2147. https://doi.org/10.1016/S0016-7037(01)00583-X.
Cioni, R., 2000. Volatile content and degassing processes in the A.D. 79 magma chamber at Vesuvius (Italy). Contrib. Mineral. Petrol. 140, 40–54. https://doi.org/10.1007/s004100000167.
Cioni, R., Bertagnini, A., Santacroce, R., Andronico, D., 2008. Explosive activity and eruption scenarios at Somma-Vesuvius (Italy): towards a new classification scheme. J. Volcanol. Geoth. Res. 178, 331–346. https://doi.org/10.1016/J.JVOLGEORES.2008.04.024.
Cioni, R., Civetta, L., Marianelli, P., Metrich, N., Santacroce, R., Sbrana, A., 1995. Compositional layering and syn-eruptive mixing of periodically refilled shallow magma chamber: the A.D. 79 Plinian eruption of Vesuvius. J. Petrol. 36, 739–776. https://doi.org/10.1093/petrology/36.3.739.
Cioni, R., Marianelli, P., Santacroce, R., 1998. Thermal and compositional evolution of the shallow magma chambers of Vesuvius: evidence from pyroxene phenocrysts and melt inclusions. J. Geophys. Res. Solid. Earth. 103, 18277–18294. https://doi.org/10.1029/98JB01124.
Cioni, R., Marianelli, P., Santacroce, R., 1999. Temperature of vesuvius magmas. Geology 27 (5), 443–446. https://doi.org/10.1130/0091-7613(1999)027<0443:TOVM>2.3.CO;2.
Cioni, R., Marianelli, P., Sbrana, A., 1990. L'eruzione del 79 d.C.: Stratigrafia dei depositi ed impatto sugli insediamenti romani nel settore orientale e meridionale del Somma-Vesuvio. In: Rivista di Studi Pompeiani vol. IV, l'Erma di Bretschneider, Italy, pp. 179–198 (in Italian).
Cioni, R., Marianelli, P., Sbrana, A., 1992. Dynamics of the A.D. 79 eruption: Stratigraphic, sedimentological and geochemical data on the successions from the Somma-Vesuvius southern and eastern sectors. Acta Vulcanol. 2, 109–123.
Cioni, R., Santacroce, R., Sbrana, A., 1999. Pyroclastic deposits as a guide for reconstructing the multi-stage evolution of the Somma-Vesuvius Caldera. Bull. Volcanol. 60, 207–222.
Civetta, L., Galati, R., Santacroce, R., 1991. Magma mixing and convective compositional layering within the Vesuvius magma chamber. Bull. Volcanol. 53, 287–300. https://doi.org/10.1007/BF00414525.
Civetta, L., Santacroce, R., 1992. Steady state magma supply in the last 3400 years of Vesuvius activity. Acta Volcanol. 2, 159–174.
Claiborne, L.L., Miller, C.F., Flanagan, D.M., Clynne, M.A., Wooden, J.L., 2010. Zircon reveals protracted magma storage and recycling beneath Mount St. Helens. Geology 38, 1011–1014. https://doi.org/10.1130/G31285.1.
Cooper, K.M., 2019. Time scales and temperatures of crystal storage in magma reservoirs: Implications for magma reservoir dynamics. Philos. T. Roy Soc. A 377, 20180009. https://doi.org/10.1098/rsta.2018.0009.
Costa, F., Dohmen, R., Chakraborty, S., 2008 Time scales of magmatic processes from modeling zoning patterns of crystals. Rev. Mineral. Geochem. 69, 545–594. https://doi.org/10.2138/rmg.2008.69.14.
Costa, F., Andreastuti, S., Bouvet de Maisonneuve, C., Pallister, J.S., 2013. Petrological insights into the storage conditions, and magmatic processes that yielded the centennial 2010 Merapi explosive eruption. J. Volcanol. Geoth. Res. 261, 209–235. https://doi.org/10.1016/j.jvolgeores.2012.12.025.
Cubellis, E., Marturano, A., 2002. Mt. Vesuvius: a macroseismic study of the earthquake of 9 October 1999. J. Volcanol. Geoth. Res. 118, 339–351. https://doi.org/10.1016/S0377-0273(02)00301-3.
Cubellis, E., Marturano, A., 2013. Felt index, source parameters and ground motion evaluation for earthquakes at Mt. Vesuvius. Ann. Geophys. 56, S0439. https://doi.org/10.4401/ag-6445.
Cubellis, E., Luongo, G., Marturano, A., 2007. Seismic hazard assessment at Mt. Vesuvius: maximum expected magnitude. J. Volcanol. Geoth. Res. 162, 139–148. https://doi.org/10.1016/j.jvolgeores.2007.03.003.
Currenti, G., Williams, C.A., 2014. Numerical modeling of deformation and stress fields around a magma chamber: constraints on failure conditions and rheology. Phys. Earth Planet. Inter. 226, 14–27. https://doi.org/10.1016/j.pepi.2013.11.003.
Dallai, L., Cioni, R., Boschi, C., D'Oriano, C., 2011. Carbonate-derived CO_2 purging magma at depth: Influence on the eruptive activity of Somma-Vesuvius, Italy. Earth Planet. Sci. Lett. 310, 84–95. https://doi.org/10.1016/j.epsl.2011.07.013.
Dal Maso, C., Marturano, A., Varone, A., 1999. Pompei, il racconto dell'eruzione. Scienze 371, 58–65 (in Italian).
De la Cruz-Reyna, S., Tárraga, M., Ortiz, R., Martínez-Bringas, A., 2010. Tectonic earthquakes triggering volcanic seismicity and eruptions. Case studies at Tungurahua and Popocatépetl volcanoes. J. Volcanol. Geoth. Res. 193 (1–2), 37–48.
Di Stefano, F., Mollo, S., Ubide, T., Petrone, C.M., Caulfield, J., Scarlato, P., Nazzari, M., Andronico, D., Del Bello, E., 2020. Mush cannibalism and disruption recorded by clinopyroxene phenocrysts at Stromboli volcano: New insights from recent 2003–2017 activity. Lithos 360–361, 105440. https://doi.org/10.1016/j.lithos.2020.105440.
Di Vito, M.A., Talamo, P., De Vita, S., Rucco, I., Zanchetta, G., Cesarano, M., 2019. Dynamics and effects of the Vesuvius Pomici di Avellino Plinian eruption and related phenomena on the Bronze Age landscape of Campania region (Southern Italy). Quat. Int. 499, 231–244.
Di Vito, M.A., Rucco, I., de Vita, S., Doronzo, D.M., Bisson, M., de' Michieli Vitturi, M., Rosi, M., Sandri, L., Zanchetta, G., Zanella, E., Costa, A., 2023. Lahar events in the last 2,000 years from Vesuvius eruptions. Part 1: distribution and impact on densely-inhabited territory estimated from field data analysis. Solid Earth 15, 405–436. https://doi.org/10.5194/se-15-405-2024.
Dohmen, R., Faak, K., Blundy, J.D., 2017. Chronometry and speedometry of magmatic processes using chemical diffusion in olivine, plagioclase and pyroxenes. Rev. Min. Geochem. 83, 535–575. https://doi.org/10.2138/rmg.2017.83.16.
Doronzo, D.M., Di Vito, M.A., Arienzo, I., Bini, M., Calusi, B., Cerminara, M., Corradini, S., de Vita, S., Giaccio, B., Gurioli, L., Mannella, G., Ricciardi, G.P., Rucco, I., Sparice, D., Todesco, M., Trasatti, E., Zanchetta, G., 2022. The 79 CE eruption of Vesuvius: a lesson from the past and the need of a multidisciplinary approach for developments in volcanology. Earth Sci. Rev. 231, 104072. https://doi.org/10.1016/j.earscirev.2022.104072.
Doronzo, D.M., Trasatti, E., Arienzo, I., Balcone-Boissard, H., Barra, D., Aiello, G., Amato, V., Di Vito, M.A., 2023. Magma reservoir growth and ground deformation preceding the 79 CE Plinian eruption of Vesuvius. Commun. Earth. Environ. 4, 211. https://doi.org/10.1038/s43247-023-00880-9.
Elms, H.C., Barker, S.J., Morgan, D.J., Wilson, C.J.N., Charlier, B.L.A., 2023. Processes and timescales of magmatic rejuvenation and residence prior to post-caldera rhyolitic eruptions: ōkataina Volcanic Centre, Aotearoa New Zealand. J. Volcanol. Geoth. Res. 437, 107790 https://doi.org/10.1016/j.jvolgeores.2023.107790.

Esposito, R., Redi, D., Danyushevsky, L.V., Gurenko, A., De Vivo, B., Manning, C.E., Bodnar, R.J., Steele-MacInnis, M., Frezzotti, M.-L., 2023. Constraining the volatile evolution of mafic melts at Mt. Somma–Vesuvius, Italy, based on the composition of reheated melt inclusions and their olivine hosts. Eur. J. Min. 35, 921–948. https://doi.org/10.5194/ejm-35-921-2023.

Federico, C., Aiuppa, A., Allard, P., Bellomo, S., Jean-Baptiste, P., Parello, F., Valenza, M., 2002. Magma-derived gas influx and water-rock interactions in the volcanic aquifer of Mt. Vesuvius, Italy. Geochim. Cosmochim. Acta 66, 963–981. https://doi.org/10.1016/S0016-7037(01)00813-4.

Falasconi, A., Petrone, C.M., Sulpizio, R., Cioni, R., 2025. Long-term precursors to large explosive eruptions of Vesuvius: evidence from the opening phase of the Avellino Plinian eruption. Bull. Volcanol. 87, 22. https://doi.org/10.1007/s00445-025-01808-1.

Fedele, L., Scarpati, C., Chiominto, G., Santangelo, I., Perrotta, A., 2025. The assembly and discharge of the Vesuvius 79 AD eruption magma chamber: new insights from petrological and chemostratigraphic evidence. J. Petrol. 66, egaf023. https://doi.org/10.1093/petrology/egaf023.

Flaherty, T., Druitt, T.H., Tuffen, H., Higgins, M.D., Costa, F., Cadoux, A., 2018. Multiple timescale constraints for high-flux magma chamber assembly prior to the late Bronze Age eruption of Santorini (Greece). Contrib. Mineral. Petr. 173, 75. https://doi.org/10.1007/s00410-018-1490-.

Fowler, S.J., Spera, F.J., 2010. A metamodel for crustal magmatism: phase equilibria of giant ignimbrites. J. Petrol. 51, 1783–1830. https://doi.org/10.1093/petrology/egq039.

Fowler, S.J., Spera, F.J., Bohrson, W.A., Belkin, H.E., De Vivo, B., 2007. Phase equilibria constraints on the chemical and physical evolution of the Campanian ignimbrite. J. Petrol 48, 459–493. https://doi.org/10.1093/petrology/egl068.

Fulignati, P., Kamenetsky, V., Marianelli, P., Sbrana, A., 2005. Fluid inclusion evidence of second immiscibility within magmatic fluids (79AD eruption of Mt. Vesuvius). Period. Min. 74, 43–54.

Fulignati, P., Marianelli, P., 2007. Tracing volatile exsolution within the 472 AD "Pollena" magma chamber of Vesuvius (Italy) from melt inclusion investigation. J. Volcanol. Geoth. Res. 161, 289–302. https://doi.org/10.1016/J.JVOLGEORES.2006.12.011.

Fulignati, P., Marianelli, P., Métrich, N., Santacroce, R., Sbrana, A., 2004. Towards a reconstruction of the magmatic feeding system of the 1944 eruption of Mt Vesuvius. J. Volcanol. Geoth. Res. 133, 13–22. https://doi.org/10.1016/S0377-0273(03)00388-3.

Galli, P., 2020. Roman to middle age earthquakes sourced by the 1980 Irpinia Fault: historical, archaeoseismological, and paleoseismological hints. Geosciences 10 (8), 286.

Gennaro, M.E., Grassa, F., Martelli, M., Renzulli, A., Rizzo, A.L., 2017. Carbon isotope composition of CO_2-rich inclusions in cumulate-forming mantle minerals from Stromboli volcano (Italy). J. Volcanol. Geoth. Res. 346, 95–103. https://doi.org/10.1016/j.jvolgeores.2017.04.001.

Gherardi, F., Barsanti, M., Principe, C., Magro, G., 2022. Helium isotopes in Plinian and inter-Plinian volcanic products of Vesuvius, Italy. Front. Earth. Sci. (Lausanne) 10, 1011203. https://doi.org/10.3389/feart.2022.1011203.

Ginibre, C., Wörner, G., Kronz, A., 2007. Crystal zoning as an archive for magma evolution. Elements 3, 261–266. https://doi.org/10.2113/gselements.3.4.261.

Giordano, G., Cas, R., Wright, J.V., 2024. Explosive eruption styles, columns, and pyroclastic fallout deposits: subaerial and subaqueous, dynamics, deposit characteristics and classification. In: Giordano, G., Cas, R., Wright, J.V. (Eds.), Volcanology: Processes, Deposits, Geology and Resources. Springer International Publishing, Cham, pp. 519–691.

Giudicepietro, F., Calabria, P., Cubellis, E., Di Prisco, C., Giacomelli, L., Macedonio, G., Martini, C., Pappalardo, L., Scandone, R., de Castris, P.L., 2025. Artistic and literary evidence of eruptive activity at Mt. Vesuvius during the apparent long quiescence period before the 1631 eruption. Sci. Rep. 15, 33235. https://doi.org/10.1038/s41598-025-18441-9.

González, G., Fujita, E., Shibazaki, B., Hayashida, T., Chiodini, G., Lucchi, F., Yokoyama, I., Nemeth, K., Mora-Amador, R., Moya, A., Chigna, G., Martí, J., Rouwet, D., 2021. Increment in the volcanic unrest and number of eruptions after the 2012 large earthquakes sequence in Central America. Sci. Rep. 11 (1), 22417. https://doi.org/10.1038/s41598-021-01725-1.

Graham, D.W., Allard, P., Kilburn, C.R.J., Spera, F.J., Lupton, J.E., 1993. Helium isotopes in some historical lavas from Mount Vesuvius. J. Volcanol. Geoth. Res. 58, 359–366. https://doi.org/10.1016/0377-0273(93)90117-A.

Graham, D.W., Lupton, J.E., 1999. Helium isotopes in historical lavas from Mount Vesuvius: Comment on 'Noble gas isotopic ratios from historical lavas and fumaroles at Mount Vesuvius' by D. Tedesco et al. Earth Planet. Sci. Lett. 174, 241–244. https://doi.org/10.1016/S0012-821X(99)00268-X.

Gualda, G.A.R., Ghiorso, M.S., Lemons, R.V., Carley, T.L., 2012. Rhyolite-MELTS: a modified calibration of MELTS optimized for silica-rich, fluid-bearing magmatic systems. J. Petrol. 53, 875–890. https://doi.org/10.1093/petrology/egr080.

Guidoboni, E. 1989. I terremoti prima del Mille in Italia e nell'area mediterranea. Storia-Geofisica-Ambiente, Istituto Nazionale di Geofisica, Italy, pp. 768 (in Italian).

Guidoboni, E., Mariotti, D., 2011. Vesuvius: Earthquakes from 1600 up to the 1631 eruption. J. Volcanol. Geoth. Res. 200, 267–272. https://doi.org/10.1016/j.jvolgeores.2010.11.021.

Gurioli, L., Cioni, R., Bertagna, C., 1999. I depositi di flusso piroclastico dell'eruzione del 79 dC caratterizzazione stratigrafica, sedimentologica e modelli di trasporto e deposizione. Atti Società Toscana Scienze Naturali, Memorie Serie. A 106, 61–72 (in Italian).

Heumann, A., Davies, G.R., Elliott, T., 2002. Crystallization history of rhyolites at Long Valley, California, inferred from combined U-series and Rb-Sr isotope systematics. Geochim. Cosmochim. Acta 66, 1821–1837. https://doi.org/10.1016/S0016-7037(01)00883-3.

Hoefs, J., 2015. Stable Isotope Geochemistry. Springer, Cham.. https://doi.org/10.1007/978-3-319-19716-6 389.

Humphreys, M.C.S., Blundy, J.D., Sparks, R.S.J., 2006. Magma evolution and open-system processes at Shiveluch Volcano: Insights from phenocryst zoning. J. Petrol. 47, 2303–2334. https://doi.org/10.1093/petrology/egl045.

Iacono-Marziano, G., Gaillard, F., Pichavant, M., 2007. Limestone assimilation and the origin of CO_2 emissions at the Alban Hills (Central Italy): Constraints from experimental petrology. J. Volcanol. Geoth. Res. 166, 91–105. https://doi.org/10.1016/j.jvolgeores.2007.07.001.

Iacono-Marziano, G., Gaillard, F., Scaillet, B., Pichavant, M., Chiodini, G., 2009. Role of non-mantle CO_2 in the dynamics of volcano degassing: the Mount Vesuvius example. Geology 37, 319–322. https://doi.org/10.1130/G25446A.1.

Jambon, A., Weber, H., Braun, O., 1986. Solubility of He, Ne, Ar, Kr and Xe in a basalt melt in the range 1250-1600℃. Geochem. Impl. Geochim. Cosmochim. Acta 50, 401–408. https://doi.org/10.1016/0016-7037(86)90193-6.

Javoy, M., Pineau, F., 1991. The volatiles record of a "popping" rock from the Mid-Atlantic Ridge at 14°N: Chemical and isotopic composition of gas trapped in the vesicles. Earth Planet. Sci. Lett. 107, 598–611. https://doi.org/10.1016/0012-821X(91)90104-P.

Jay, G., 2024. Volcanic eruption. In: Ciottone, G. (Ed.), Ciottone's Disaster Medicine. Third Edition. Elsevier, New Delhi, pp. 631–636. https://doi.org/10.1016/B978-0-323-80932-0.00102-6.

Joron, J. L., Me□trich, N., Rosi, M., Santacroce, R., Sbrana, A., 1987. Chemistry and petrography. In: Santacroce, R. (Ed.), Somma-Vesuvius. Quaderni de 'La Ricerca Scientifica 114. Italy, pp. 105–174.

Kahl, M., Chakraborty, S., Costa, F., Pompilio, M., 2011. Dynamic plumbing system beneath volcanoes revealed by kinetic modelling and the connection to monitoring data: an example from Mt Etna. Earth Planet Sci. Lett. 308, 11–22. https://doi.org/10.1016/j.epsl.2011.05.008.

Kahl, M., Chakraborty, S., Costa, F., Pompilio, M., Liuzzo, M., Viccaro, M., 2013. Compositionally zoned crystals and realtime degassing data reveal changes in magma transfer dynamics during the 2006 summit eruptive episodes of Mt. Etna. Bull Volcanol 75, 692. https://doi.org/10.1007/s00445-013-0692-7.

Kahl, M., Chakraborty, S., Pompilio, M., Costa, F., 2015. Constraints on the nature and evolution of the magma plumbing system of Mt. Etna volcano (1991-2008) from a combined thermodynamic and kinetic modelling of the compositional record of minerals. J. Petrol. 56, 2025–2068. https://doi.org/10.1093/petrology/egv063.

Kilgour, G.N., Saunders, K.E., Blundy, J.D., Cashman, K.V., Scott, B.J., Miller, C.A., 2014. Timescales of magmatic processes at Ruapehu volcano from diffusion chronometry and their comparison to monitoring data. J. Volcanol. Geoth. Res. 288, 62–75. https://doi.org/10.1016/j.jvolgeores.2014.09.010.

Lages, J., Rizzo, A.L., Aiuppa, A., Robidoux, P., Aguilar, R., Apaza, F., Masias, P., 2021. Crustal controls on light noble gas isotope variability along the Andean Volcanic Arc. Geochem. Perspect. Lett. 19, 45–49.

Landi, P., Bertagnini, A., Rosi, M., 1999. Chemical zoning and crystallization mechanisms in the magma chamber of the Pomici di Base plinian eruption of Somma-Vesuvius (Italy). Contrib. Mineral. Petrol. 135, 179–197. https://doi.org/10.1007/s004100050505.

Latter, J.H., 1971. The interdependence of seismic and volcanic phenomena: some space—time relationships in seismicity and volcanism. Bull. Volcanol. 35 (1), 127–142.

Legrand, D., 2022. Which earthquake can trigger a volcanic eruption? J. Volcanol. Geoth. Res. 432, 107698.

Lima, A., De Vivo, B., Fedele, L., Sintoni, F., Milia, A., 2007. Geochemical variations between the 79 AD and 1944 AD Somma-Vesuvius volcanic products: constraints on the evolution of the hydrothermal system based on fluid and melt inclusions. Chem. Geol. 237, 401–417. https://doi.org/10.1016/j.chemgeo.2006.07.011.

Lo Forte, F.M., Boudoire, G., Frezzotti, M.L., Rotolo, S.G., Sandoval-Velasquez, A., Viveiros, F., Zanon, V., Aiuppa, A., Rizzo, A.L., 2024. The helium and carbon isotopic signature of Ocean island basalts: Insights from Fogo volcano (Cape Verde archipelago). Earth Planet. Sci. Lett. 645, 118930. https://doi.org/10.1016/j.epsl.2024.118930.

Macpherson, C., Mattey, D., 1994. Carbon isotope variations of CO_2 in Central Lau Basin basalts and ferrobasalts. Earth Planet. Sci. Lett. 121, 263–276. https://doi.org/10.1016/0012-821X(94)90072-8.

Mangler, M.F., Petrone, C.M., Hill, S., Delgado-Granados, H., Prytulak, J., 2020. A pyroxenic view on magma hybridization and crystallization at Popocatépetl Volcano, Mexico. Front. Earth. Sci. 8, 362. https://doi.org/10.3389/feart.2020.00362.

Marianelli, P., Métrich, N., Santacroce, R., Sbrana, A., 1995. Mafic magma batches at Vesuvius: a glass inclusion approach to the modalities of feeding stratovolcanoes. Contrib. Mineral. Petr. 120, 159–169. https://doi.org/10.1007/BF00287113.

Marianelli, P., Métrich, N., Sbrana, A., 1999. Shallow and deep reservoirs involved in magma supply of the 1944 eruption of Vesuvius. Bull. Volcanol. 61, 48–63. https://doi.org/10.1007/s004450050262.

Marianelli, P., Sbrana, A., Métrich, N., Cecchetti, A., 2005. The deep feeding system Vesuvius involved in recent violent strombolian eruptions. Geophys. Res. Lett. 32, L02306. https://doi.org/10.1029/2004GL021667.

Martelli, M., Nuccio, P.M., Stuart, F.M., Burgess, R., Ellam, R.M., Italiano, F., 2004. Helium–strontium isotope constraints on mantle evolution beneath the Roman Comagmatic Province, Italy. Earth Planet. Sci. Lett. 224, 295–308. https://doi.org/10.1016/j.epsl.2004.05.025.

Martí, J., 2024. From rest to eruption: how we should anticipate volcanic eruptions. NPJ Nat. Hazards 1, 31.

Martí, J., Pinel, V., López, C., Geyer, A., Abella, R., Tárraga, M., Blanco, M.J., Castro, A., Rodríguez, C., 2013. Causes and mechanisms of the 2011–2012 El Hierro (Canary Islands) submarine eruption. J. Geophys. Res. Solid. Earth. 118, 823–839. https://doi.org/10.1002/jgrb.50087.

Marturano, A., Rinalsis, V., 1998. Seismicity before the 79 AD Vesuvius eruption. In: Albore, L.C., Ortolano, F. B. (Eds.), Il sistema uomo ambiente tra passato e presente, CUEBC - Territorio storico ed ambiente, Italy, pp 322 (in Italian).

Marturano, A., 2006. Geophysical precursors at Vesuvius from historical and archeological sources. In: Marturano, A. (Ed.), Developments in Volcanology. Elsevier, pp. 249–263.

Marturano, A., 2008. Sources of ground movement at Vesuvius before the AD 79 eruption: evidence from contemporary accounts and archaeological studies. J. Volcanol. Geoth. Res. 177, 959–970. https://doi.org/10.1016/j.jvolgeores.2008.07.017.

Marty, B., Jambon, A., 1987. C/^{3}He in volatile fluxes from the solid Earth: Implications for carbon geodynamics. Earth Planet. Sci. Lett. 83, 16–26. https://doi.org/10.1016/0012-821X(87)90047-1.

Marzocchi, W., 2002. Remote seismic influence on large explosive eruptions. J. Geophys. Res. [Solid Earth] 107 (B1), EPM–6.

Marzocchi, W., Scandone, R., Mulargia, F., 1993. The tectonic setting of Mount Vesuvius and the correlation between its eruptions and the earthquakes of the Southern Apennines. J. Volcanol. Geoth. Res. 58 (1–4), 27–41.

Masotta, M., Mollo, S., Freda, C., Gaeta, M., Moore, G., 2013. Clinopyroxene–liquid thermometers and barometers specific to alkaline differentiated magmas. Contrib. Min. Petr. 166, 1545–1561. https://doi.org/10.1007/s00410-013-0927-9.

Mattey, D.P., 1991. Carbon dioxide solubility and carbon isotope fractionation in basaltic melt. Geochim. Cosmochim. Acta 55, 3467–3473. https://doi.org/10.1016/0016-7037(91)90508-3.

Melluso, L., Scarpati, C., Zanetti, A., Sparice, D., de' Gennaro, R., 2022. The petrogenesis of chemically zoned, phonolitic, Plinian and sub-Plinian eruptions of Somma-Vesuvius, Italy: Role of accessory phase removal, independently filled magma reservoirs with time, and transition from slightly to highly silica undersaturated magmatic series in an ultrapotassic stratovolcano. Lithos 430–431, 106854. https://doi.org/10.1016/j.lithos.2022.106854.

Morgan, D.J., Blake, S., Rogers, N.M., De Vivo, B., Rolandi, G., Davidson, J.P., 2006. Magma chamber recharge at Vesuvius in the century prior to the eruption of A. D. 79. Geology 34, 845–848. https://doi.org/10.1130/G22604.1.

Morgan, D.J., Blake, S., Rogers, N.W., DeVivo, B., Rolandi, G., Macdonald, R., Hawkesworth, C.J., 2004. Time scales of crystal residence and magma chamber volume from modelling of diffusion profiles in phenocrysts: Vesuvius 1944. Earth Planet. Sci. Lett. 222, 933–946. https://doi.org/10.1016/j.epsl.2004.03.030.

Müller, T., Dohmen, R., Becker, H.W., ter Heege, J.H., Chakraborty, S., 2013. Fe–Mg interdiffusion rates in clinopyroxene: experimental data and implications for Fe–Mg exchange geothermometers. Contrib. Min. Petrol. 166, 1563–1576. https://doi.org/10.1007/s00410-013-0941-y.

Nardini, N., Casetta, F., Petrone, C.M., Buret, Y., Ntaflos, T., Coltorti, M., 2024. Modelling ancient magma plumbing systems through clinopyroxene populations: a case study from Middle Triassic volcanics (Dolomites, Italy). Contrib. Mineral. Petr. 179, 22. https://doi.org/10.1007/s00410-024-02102-7.

Nostro, C., Stein, R.S., Cocco, M., Belardinelli, M.E., Marzocchi, W., 1998. Two-way coupling between Vesuvius eruptions and southern Apennine earthquakes, Italy, by elastic stress transfer. J. Geophys. Res. [Solid Earth] 103 (B10), 24487–24504.

Nishimura, T., 2017. Triggering of volcanic eruptions by large earthquakes. Geophys. Res. Lett. 44, 7750–7756. https://doi.org/10.1002/2017GL074579.

Nunziata, C., Natale, M., Luongo, G., Panza, F., G.,, 2006. Magma reservoir at Mt. Vesuvius: size of the hot, partially molten, crust material detected deeper than 8 km. Earth Planet. Sci. Lett. 242, 51–57. https://doi.org/10.1007/s00410-024-02102-7.

Ostorero, L., Balcone-Boissard, H., Boudon, G., Shapiro, N.M., Belousov, A., Belousova, M., Auer, A., Senyukov, S.L., Droznina, S.Y., 2022. Correlated petrology and seismicity indicate rapid magma accumulation prior to eruption of Kizimen volcano, Kamchatka. Commun. Earth. Environ. 3, 290. https://doi.org/10.1038/s43247-022-00622-3.

Ostorero, L., Boudon, G., Balcone-Boissard, H., Martel, C., Erdmann, S., Morgan, D.J., d'Augustin, T., 2025. The 1956 eruption of Bezymianny volcano (Kamchatka). Part II—Magma dynamics and timescales from crystal records. Bull. Volcanol. 87 (3), 19.

Palummo, F., Mollo, S., Petrone, C.M., Ellis, B.S., De Astis, G., Nazzari, M., Scarlato, P., Bachmann, O., 2021. Decoding multiple zoning patterns in clinopyroxene phenocrysts at Vulcano Island: a record of dynamic crystallization through interconnected reservoirs. Lithos 406–407, 106517. https://doi.org/10.1016/j.lithos.2021.106517.

Paonita, A., Federico, C., Bonfanti, P., Capasso, G., Inguaggiato, S., Italiano, F., Madonia, P., Pecoraino, G., Sortino, F., 2013. The episodic and abrupt geochemical changes at La Fossa fumaroles (Vulcano Island, Italy) and related constraints on the dynamics, structure, and compositions of the magmatic system. Geochim. Cosmochim. Acta 120, 158–178. https://doi.org/10.1016/j.gca.2013.06.015.

Pappalardo, L., Mastrolorenzo, G., 2010. Short residence times for alkaline Vesuvius magmas in a multi-depth supply system: Evidence from geochemical and textural studies. Earth Planet. Sci. Lett. 296 (1), 133–143. https://doi.org/10.1016/j.epsl.2010.05.010.

Pappalardo, L., Ottolini, L., Mastrolorenzo, G., 2008. The Campanian Ignimbrite (southern Italy) geochemical zoning: insight on the generation of a super-eruption from catastrophic differentiation and fast withdrawal. Contrib. Mineral. Petrol. 156, 1–26. https://doi.org/10.1007/s00410-007-0270-0.

Passarelli, L., Brodsky, E.E., 2012. The correlation between run-up and repose times of volcanic eruptions. Geophys. J. Int. 188, 1025–1045. https://doi.org/10.1111/j.1365-246X.2011.05298.x.

Pelullo, C., Chakraborty, S., Cambeses, A., Dohmen, R., Arienzo, I., D'Antonio, M., Pappalardo, L., Petrosino, P., 2022. Insights into the temporal evolution of magma plumbing systems from compositional zoning in clinopyroxene crystals from the Agnano-Monte Spina Plinian eruption (Campi Flegrei, Italy). Geochim. Cosmochim. Acta 328, 185–206. https://doi.org/10.1016/j.gca.2022.04.007.

Pelullo, C., Chakraborty, S., Montagna, C.P., Arienzo, I., Brown, R.J., D'Antonio, M., de Vita, S., D'Oriano, C., Nazzari, M., Pappalardo, L., Petrosino, P., 2024. A multi-methodological approach to record dynamics and timescales of the plumbing system of Zaro (Ischia Island, Italy). Contrib. Mineral. Petr. 179, 54. https://doi.org/10.1007/s00410-024-02138-9.

Petrone, C.M., Braschi, E., Francalanci, L., Casalini, M., Tommasini, S., 2018. Rapid mixing and short storage timescale in the magma dynamics of a steady-state volcano. Earth Planet. Sci. Lett. 492, 206–221. https://doi.org/10.1016/j.epsl.2018.03.055.

Petrone, C.M., Bugatti, G., Braschi, E., Tommasini, S., 2016. Pre-eruptive magmatic processes re-timed using a non-isothermal approach to magma chamber dynamics. Nat Commun 7, 12946. https://doi.org/10.1038/ncomms12946.

Petrone, C.M., Mollo, S., Gertisser, R., Buret, Y., Scarlato, P., Del Bello, E., Andronico, D., Ellis, B., Pontesilli, A., De Astis, G., Giacomoni, P.P., Coltorti, M., Reagan, M., 2022. Magma recharge and mush rejuvenation drive paroxysmal activity at Stromboli volcano. Nat. Commun. 13, 7717. https://doi.org/10.1038/s41467-022-35405-z.

Piana Agostinetti, N., Amato, A., 2009. Moho depth and Vp/Vs ratio in peninsular Italy from teleseismic receiver functions. J. Geophys. Res. 114 (B6), B06303. https://doi.org/10.1029/2008JB005899.

Pichavant, M., Scaillet, B., Pommier, A., Iacono-Marziano, G., Cioni, R., 2014. Nature and evolution of primitive Vesuvius magmas: an experimental study. J. Petrol. 55, 2281–2310. https://doi.org/10.1093/petrology/egu057.

Piochi, M., Ayuso, R.A., De Vivo, B., Somma, R., 2006. Crustal contamination and crystal entrapment during polybaric magma evolution at Mt. Somma–Vesuvius volcano, Italy: Geochemical and Sr isotope evidence. Lithos 86, 303–329. https://doi.org/10.1016/j.lithos.2005.05.009.

Polo-Sánchez, A., Flaherty, T., Hervé, G., Druitt, T., Fabbro, G.N., Nomikou, P., Balcone-Boissard, H., 2023. Tracking timescales of magma reservoir recharge through caldera cycles at Santorini (Greece). Emphasis on an explosive eruption of Kameni Volcano. Front. Earth. Sci. 11, 1128083. https://doi.org/10.3389/feart.2023.1128083.

Rizzo, A.L., Caracausi, A., Chavagnac, V., Nomikou, P., Polymenakou, P.N., Mandalakis, M., Kotoulas, G., Magoulas, A., Castillo, A., Lampridou, D., 2016. Kolumbo submarine volcano (Greece): an active window into the Aegean subduction system. Sci. Rep. 6, 28013. https://doi.org/10.1038/srep28013.

Rizzo, A.L., Faccini, B., Casetta, F., Faccincani, L., Ntaflos, T., Italiano, F., Coltorti, M., 2021. Melting and metasomatism in West Eifel and Siebengebirge Sub-Continental Lithospheric Mantle: evidence from concentrations of volatiles in fluid inclusions and petrology of ultramafic xenoliths. Chem. Geol. 581, 120400. https://doi.org/10.1016/j.chemgeo.2021.120400.

Rosi, M., Acocella, V., Cioni, R., Bianco, F., Costa, A., De Martino, P., Giordano, G., Inguaggiato, S., 2022. Defining the pre-eruptive states of active volcanoes for improving eruption forecasting. Front. Earth Sci. 10, 795700. https://doi.org/10.3389/feart.2022.795700.

Rosi, M., Principe, C., Vecci, R., 1993. The 1631 Vesuvius eruption. a reconstruction based on historical and stratigraphical data. J. Volcanol. Geoth. Res. 58, 151–182. https://doi.org/10.1016/0377-0273(93)90106-2.

Sandoval-Velasquez, A., Casetta, F., Ntaflos, T., Aiuppa, A., Coltorti, M., Frezzotti, M. L., Alonso, M., Padrón, E., Pankhurst, M., Pérez, N.M., Rizzo, A.L., 2024. 2021 Tajogaite eruption records infiltration of crustal fluids within the upper mantle beneath La Palma, Canary Islands. Front. Earth. Sci. 12, 1303872. https://doi.org/10.3389/feart.2024.1303872.

Sano, Y., Marty, B., 1995. Origin of carbon in fumarolic gas from island arcs. Chem. Geol. 119, 265–274. https://doi.org/10.1016/0009-2541(94)00097-R.

Santacroce, R., Bertagnini, A., Civetta, L., Landi, P., Sbrana, A., 1993. Eruptive dynamics and petrogenetic processes in a very shallow magma reservoir: the 1906 eruption of Vesuvius. J. Petrol. 34, 383–425. https://doi.org/10.1093/petrology/34.2.383.

Santacroce, R., Cioni, R., Marianelli, P., Sbrana, A., Sulpizio, R., Zanchetta, G., Donahue, D.J., Joron, J.L., 2008. Age and whole rock-glass compositions of proximal pyroclastics from the major explosive eruptions of Somma-Vesuvius: a review as a tool for distal tephrostratigraphy. J. Volcanol. Geoth. Res. 177, 1–18. https://doi.org/10.1016/j.jvolgeores.2008.06.009.

Saunders, K., Blundy, J., Dohmen, R., Cashman, K., 2012. Linking petrology and seismology at an active volcano. Science 1979 (336), 1023–1027. https://doi.org/10.1126/science.1220066.

Sautter, V., Jaoul, O., Abel, F., 1988. Aluminum diffusion in diopside using the $^{27}Al(p,\gamma)^{28}Si$ nuclear reaction: preliminary results. Earth Planet. Sci. Lett. 89, 109–114.
Sbrana, A., Cioni, R., Marianelli, P., Sulpizio, R., Andronico, D., Pasquini, G., 2020. Volcanic evolution of the Somma-Vesuvius complex (Italy). J. Maps 16, 137–147. https://doi.org/10.1080/17445647.2019.1706653.
Scaillet, B., Pichavant, M., Cioni, R., 2008. Upward migration of Vesuvius magma chamber over the past 20,000 years. Nature 455, 216–219. https://doi.org/10.1038/nature07232.
Scandone, R., Giacomelli, L., 2008. Precursors of eruptions at Vesuvius (Italy). J. Volcanol. Geoth. Res. 171, 191–200. https://doi.org/10.1016/j.jvolgeores.2007.11.018.
Scandone, R., Giacomelli, L., Speranza, F., 2008. Persistent activity and violent strombolian eruptions at Vesuvius between 1631 and 1944. J. Volcanol. Geoth. Res. 170 (3–4), 167–180.
Scarpati, C., Chiominto, G., Santangelo, I., Perrotta, A., Fedele, L., 2024. The AD 79 Vesuvius eruption revisited: Plinian and post-Plinian falls. J. Geol. Soc. London 182 (1), jgs2024-071. https://doi.org/10.1144/jgs2024-071.
Scarpati, C., Santangelo, I., Chiominto, G., Perrotta, A., Branney, M.J., Fedele, L., 2024. The AD 79 Vesuvius eruption revisited: the pyroclastic density currents. J. Geol. Soc. London 182 (1), jps2024-072. https://doi.org/10.1144/jgs2024-072.
Scheibner, B., Heumann, A., Wörner, G., Civetta, L., 2008. Crustal residence times of explosive phonolite magmas: U–Th ages of magmatic Ca-Garnets of Mt. Somma-Vesuvius (Italy). Earth Planet. Sci. Lett. 276, 293–301. https://doi.org/10.1016/j.epsl.2008.09.028.
Segall, P., 2019. Magma chambers: what we can, and cannot, learn from volcano geodesy. Phil. Trans. R. Soc. A 377 (2139), 20180158.
Self, S., 2006. The effects and consequences of very large explosive volcanic eruptions. Philos. Trans. A Math. Phys. Eng. Sci. 364 (1845), 2073–2097. https://doi.org/10.1098/rsta.2006.1814.
Shapiro, N.M., Droznin, D.V., Droznina, S.Y., Senyukov, S.L., Gusev, A.A., Gordeev, E.I., 2017. Deep and shallow long-period volcanic seismicity linked by fluid-pressure transfer. Nat- Geosci. 10, 442–445.
Sigurdsson, H., Carey, S., Cornell, W., Pescatore, T., 1985. The eruption of Vesuvius in A.D. 79. Nat. Geogr. Res. 3, 332–397.
Sigurdsson, H., Cornell, W., Carey, S., 1990. Influence of magma withdrawal on compositional gradients during the AD 79 Vesuvius eruption. Nature 345, 519–521. https://doi.org/10.1038/345519a0.
Sigmundsson, F., Parks, M., Pedersen, R., Jónsdóttir, K., Ófeigsson, B.G., Grapenthin, R., Dumont, S., Einarsson, P., Drouin, V., Heimisson, E.R., Hjartardóttir, Á.R., Guðmundsson, M., Geirsson, H., Hreinsdóttir, S., Sturkell, E., Hooper, A., Högnadóttir, Þ., Vogfjörð, K., Barnie, T., Roberts, M.J., 2018. Magma movements in volcanic plumbing systems and their associated ground deformation and seismic patterns. In: Burchardt, S. (Ed.), Volcanic and Igneous Plumbing Systems. Elsevier, pp. 285–322.
Solaro, C., Balcone-Boissard, H., Morgan, D.J., Boudon, G., Martel, C., Ostorero, L., 2020. A system dynamics approach to understanding the deep magma plumbing system beneath Dominica (Lesser Antilles). Front. Earth. Sci. 8, 574032. https://doi.org/10.3389/feart.2020.574032.
Sparice, D., Di Vito, M.A., Amato, V., Amoretti, V., Russo, A., Talamo, P., Zuchtriegel, G., 2025. Unveiling the volcanic history of ancient Pompeii (Italy): New insights from the Late Pleistocene to Holocene (Pre-79 CE) stratigraphy. Quaternary 8 (1), 4.
Sparks, R.S.J., Cashman, K.V., 2017. Dynamic magma systems: Implications for forecasting volcanic activity. Elements 13, 35–40. https://doi.org/10.2113/gselements.13.1.35.
Streck, M.J., 2008. Mineral textures and zoning as evidence for open system processes. Rev. Mineral. Geochem. 69, 595–622. https://doi.org/10.2138/rmg.2008.69.15.
Tedesco, D., Allard, P., Sano, Y., Wakita, H., Pece, R., 1990. Helium-3 in subaerial and submarine fumaroles of Campi Flegrei caldera, Italy. Geochim. Cosmochim. Acta 54, 1105–1116. https://doi.org/10.1016/0016-7037(90)90442-N.
Trepmann, C.A., Stockhert, B., Chakraborty, S., 2004. Oligocene trondhjemitic dikes in the Austroalpine basement of the Pfunderer Berge, Südtirol - level of emplacement and metamorphic overprint. Eur. J. Mineral. 16, 641–659. https://doi.org/10.1127/0935-1221/2004/0016-0641.
Trigila, R., De Benedetti, A.A., 1993. Petrogenesis of Vesuvius historical lavas constrained by Pearce element ratios analysis and experimental phase equilibria. J. Volcanol. Geoth. Res. 58, 315–343. https://doi.org/10.1016/0377-0273(93)90115-8.
Turner, S., Costa, F., 2007. Measuring timescales of magmatic evolution. Elements 3, 267–272. https://doi.org/10.2113/gselements.3.4.267.
Ubide, T., Mollo, S., Zhao, J.X., Nazzari, M., Scarlato, P., 2019. Sector-zoned clinopyroxene as a recorder of magma history, eruption triggers, and ascent rates. Geochim. Cosmochim. Acta 251, 265–283. https://doi.org/10.1016/J.GCA.2019.02.021.
Vazquez, J.A., Reid, M.R., 2004. Probing the accumulation history of the voluminous Toba magma. Science 305 (5686), 991–994. https://doi.org/10.1126/science.1096994.
Walter, T.R., Amelung, F., 2007. Volcanic eruptions following M≥ 9 megathrust earthquakes: Implications for the Sumatra-Andaman volcanoes. Geology 35 (6), 539–542.
Watt, S.F., Pyle, D.M., Mather, T.A., 2009. The influence of great earthquakes on volcanic eruption rate along the Chilean subduction zone. Earth Planet. Sci. Lett. 277 (3–4), 399–407.
Weber, G., Arce, J.L., Ulianov, A., Caricchi, L., 2019. A recurrent magmatic pattern on observable timescales prior to Plinian eruptions from Nevado de Toluca (Mexico). J. Geophys. Res. Solid. Earth. 124, 10999–11021. https://doi.org/10.1029/2019JB017640.
Wotzlaw, J.-F., Bastian, L., Guillong, M., Forni, F., Laurent, O., Neukampf, J., Sulpizio, R., Chelle-Michou, C., Bachmann, O., 2022. Garnet petrochronology reveals the lifetime and dynamics of phonolitic magma chambers at Somma-Vesuvius. Sci. Adv. 8, eabk2184. https://doi.org/10.1126/sciadv.abk2184.
Zanon, V., Cyrzan, K., D'Auria, L., Pankhurst, M., Rodríguez, F., Coldwell, B., Martín-Lorenzo, A., 2022. The magma ascent path during the 2021 eruption of Cumbre Vieja (La Palma Island, Canary archipelago) highlighted by fluid inclusions and seismicity. EGU General Assembly 2022, Vienna, Austria, 23–27 May 2022, EGU22-10203. https://doi.org/10.5194/egusphere-egu22-10203.
Zanon, V., Schiavi, F., Cyrzan, K., Pankhurst, M.J., 2024. Toward a near real-time magma ascent monitoring by combined fluid inclusion barometry and ongoing seismicity. Sci. Adv. 10, eadi4300.